



HAL
open science

Structural classification of boron nitride twisted bilayers and ab initio investigation of their stacking-dependent electronic structure

Sylvain Latil, Hakim Amara, Lorenzo Sponza

► To cite this version:

Sylvain Latil, Hakim Amara, Lorenzo Sponza. Structural classification of boron nitride twisted bilayers and ab initio investigation of their stacking-dependent electronic structure. *SciPost Physics*, In press. hal-03962777v1

HAL Id: hal-03962777

<https://hal.science/hal-03962777v1>

Submitted on 30 Jan 2023 (v1), last revised 27 Apr 2023 (v2)

HAL is a multi-disciplinary open access archive for the deposit and dissemination of scientific research documents, whether they are published or not. The documents may come from teaching and research institutions in France or abroad, or from public or private research centers.

L'archive ouverte pluridisciplinaire **HAL**, est destinée au dépôt et à la diffusion de documents scientifiques de niveau recherche, publiés ou non, émanant des établissements d'enseignement et de recherche français ou étrangers, des laboratoires publics ou privés.

Structural classification of boron nitride twisted bilayers and ab initio investigation of their stacking-dependent electronic structure

Sylvain Latil¹, Hakim Amara^{2,3} and Lorenzo Sponza^{2,4}

¹ Université Paris-Saclay, CEA, CNRS, SPEC, 91191 Gif-sur-Yvette, France

² Université Paris-Saclay, ONERA, CNRS, Laboratoire d'étude des microstructures (LEM), 92322, Châtillon, France

³ Université Paris Cité, Laboratoire Matériaux et Phénomènes Quantiques (MPQ), CNRS-UMR7162, 75013 Paris, France

⁴ European Theoretical Spectroscopy Facility (ETSF), B-4000 Sart Tilman, Liège, Belgium

Abstract

Since the discovery of superconductive twisted bilayer graphene which initiated the field of twistrionics, moiré systems have not ceased to exhibit fascinating properties. We demonstrate that in boron nitride twisted bilayers, for a given moiré periodicity, there are five different stackings which preserve the monolayer hexagonal symmetry (i.e. the invariance upon rotations of 120°) and not only two as always discussed in literature. We introduce some definitions and a nomenclature that identify unambiguously the twist angle and the stacking sequence of any hexagonal bilayer with order-3 rotation symmetry. Moreover, we employ density functional theory to study the evolution of the band structure as a function of the twist angle for each of the five stacking sequences of boron nitride bilayers. We show that the gap is indirect at any angle and in any stacking, and identify features that are conserved within the same stacking sequence irrespective of the angle of twist.



Copyright S. Latil *et al.*

This work is licensed under the Creative Commons

[Attribution 4.0 International License](https://creativecommons.org/licenses/by/4.0/).

Published by the SciPost Foundation.

Received 29-08-2022

Accepted 02-12-2022

Published ??-??-20??

doi:[10.21468/SciPostPhys.?.?.??](https://doi.org/10.21468/SciPostPhys.?.?.??)

1

2 Contents

3	1 Geometrical analysis	3
4	2 Electronic structure	5
5	3 Conclusions	10
6	A Asymmetric honeycomb supercells	10
7	B Stacking geometries	12
8	C Moiré stacking angles	13
9	D Redundancy of the case ($p - q = 3t$)	15

10	E Completeness of the description with (q, p) pairs	16
11	F Layer groups of moiré structures	17
12	G Computational details	19
13	H Untwisted bilayers	20
14	I Nearly-free-electron states	21
15	J Band gap of the $\delta = 2$ family	23
16	K Band structure of the other stackings	24
17	References	25

20 Initiated by twisted bilayer graphene, moiré systems formed of 2D atomic layers have
21 recently been established as a unique playground for highlighting novel and fascinating prop-
22 erties [1]. A tiny twist between the two van der Waals atomic layers can modify deeply their
23 electronic properties as a consequence of the flattening of the band dispersion. In graphene, a
24 flat moiré mini-band appears at specific “magic angles” [2, 3] whose occupation drives super-
25 conductive/insulating transitions which open new perspectives on the investigation of strong
26 correlation in 2D systems [4–6]. In gapped twisted bilayers (e.g. semiconducting transition
27 metal dichalcogenides) the moiré bands have an impact on the optical properties. For instance,
28 by varying the twist angle it is possible to modulate the exciton lifetime [7], or the energy and
29 intensity of emitted light [8–11]. In these systems, flat bands give rise to intriguing phenomena
30 without the need of being twisted by specific “magic” angles [12–14].

31 Hexagonal boron nitride (hBN) is a cardinal compound in 2D materials research. Used
32 mostly as encapsulating layer, it has nonetheless attracting properties on its own respect,
33 mainly because of its large band gap (> 6 eV) [15, 16] which is at the origin of a strong
34 UV emission [17, 18], single photon emission [19–24] and its application as gating layer in 2D
35 electronics [25–28]. Recently ferroelectricity has been enabled in twisted hBN bilayers, thus
36 expanding further its range of applications [29, 30]. In the bulk phase and in thin layers its
37 optical properties are driven by excitons [31]. In hBN moiré systems, Lee and coworkers [32]
38 observed an increase of the luminescence intensity and a decrease of the sub-band gapwidth
39 for increasing twist angles. From the standpoint of atomistic simulations, geometries with
40 small rotation angles require very large periodic cells (order of thousands of atoms) which
41 are out of reach for most self-consistent numerical approaches [33]. As for graphene [2, 34],
42 tight-binding or continuous models based on the $k \cdot p$ approximation are more adapted to deal
43 with very large systems and have therefore been developed [6, 14, 35, 36]. However these
44 studies are incomplete on two aspects. First, the very nature of the band gap is still not elu-
45 cidated while it obviously rules the optical and excitonic properties of monolayer and bulk
46 hBN [15, 16, 37]. Second, the stacking sequence in bilayers is seldom considered and, when it
47 has been, only two geometries were taken into account [33, 36]. Yet, it has been shown that
48 the stacking sequence strongly influences the character of the gap [31, 38, 39] through long
49 range interplanar interactions.

50 In this Letter, we investigate the electronic structure of twisted hBN bilayers by taking into
51 account fully and on the same footing its dependence on the twist angle and the stacking
52 sequence. As a first step, we demonstrate the existence of five and only five different stacking
53 possibilities to construct hBN bilayers with hexagonal symmetry and provide a non-ambiguous

54 nomenclature applicable to untwisted configurations as well and to any other homobilayer
 55 formed of hexagonal 2D materials. Stemming from this symmetry analysis, we employed
 56 density functional theory (DFT) to investigate the evolution of the band structure as a function
 57 of the twist angle for each of the five stackings.

58 1 Geometrical analysis

59 To construct a tiling of rotated bilayers preserving long range translational symmetries, we first
 60 define coincident supercells [40, 41]. Let us take a honeycomb lattice with primitive vectors
 61 \mathbf{a}_1 and \mathbf{a}_2 forming an angle of 60° and with the two atoms of the cell separated by τ . Then we
 62 define the (q, p) hexagonal supercell as resulting from the vectors $\mathbf{A}_i^{(q,p)} = \sum_j M_{ij}^{(q,p)} \mathbf{a}_j$ defined
 63 by means of the matrix

$$M^{(q,p)} = \begin{bmatrix} q & p \\ -p & p+q \end{bmatrix}. \quad (1)$$

64 Similarly we use equation (1) to introduce the (p, q) and the $(-q, p+q)$ supercells. The re-
 65 sulting twist angles are given respectively by the formulae:

$$\tan \theta = \frac{\sqrt{3}(p^2 - q^2)}{p^2 + q^2 + 4pq} \quad \text{or} \quad \tan \theta' = \frac{\sqrt{3}(q^2 + 2pq)}{2p^2 - q^2 + 2pq}.$$

66 The supercells defined above and the resulting twist angles are sketched in Figure 1.a.

67 The p and q integers obey to some constraints: they must be different and non zero,
 68 otherwise they lead to twist angles of 0° or 60° , they must have no common divisor, and the
 69 case $p - q$ multiple of 3 has to be excluded as it corresponds to non-primitive moiré supercells.
 70 Moreover, since twist angles are defined modulo 60° , the definition of the M matrix is not
 71 unique. We will then restrict ourselves arbitrarily to cases $p > q$ which imply that angles are
 72 positive and $\theta + \theta' = 60^\circ$. Note finally that the notation introduced here for twisted bilayers can
 73 be employed also for untwisted structures taking $q = 0$ and $p = 1$. Despite these constraints
 74 and arbitrary choices, we demonstrate in Appendix E that all twisted angles corresponding to
 75 periodic moiré patterns can be expressed through an appropriate choice of the (q, p) pair.

76 Stacking the correct supercells is not enough to construct moiré hexagonal bilayers because
 77 the respective alignment is also crucial. Let us introduce a subscript labelling the origin of the
 78 supercell (B = boron, N = nitrogen, H = hexagon center). Without loss of generality we will
 79 always consider the supercell of the lower layer as being $(q, p)_B$ (cfr. Figure 1b) while that

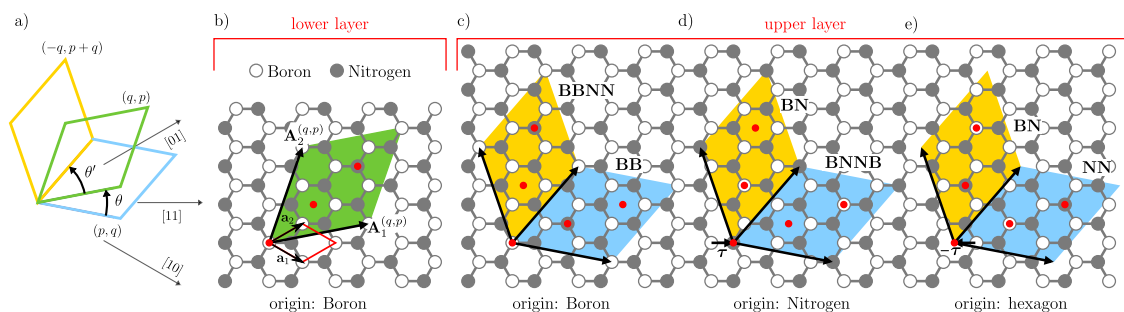


Figure 1: a) Graphical representation of θ and θ' angles according to the $\{p, q\}$ integers. b) The lower layer supercell is $(q, p)_B$. c) d) and e) The supercells of the upper layer $(p, q)_X$ with $X = B, N$ or H respectively are drawn in blue, and the corresponding $(-q, p+q)_X$ supercells in yellow. High symmetry points are reported as red dots. In the examples $p = 2$ and $q = 1$.

80 of the upper layer can be any of $(p, q)_{B,N,H}$ or $(-q, p + q)_{B,N,H}$. As a consequence, one ends
 81 up with six bilayers listed in Table 1 and sketched in panels c), d) and e) of Figure 1 for the
 82 case $p = 2, q = 1$. In each supercell there are three direct-space high-symmetry points (red
 83 bullets in Figure 1): the points $(0, 0)$, $(1/3, 1/3)$ and $(2/3, 2/3)$ in the supercell reduced
 84 coordinates. Depending on the coincident atoms in these points, one can distinguish between
 85 (i) two geometries with a double sublattice coincidence per cell, the $(p, q)_N$ and the $(-q, p + q)_B$
 86 ones, with a twist angle $-\theta'$, and (ii) the remaining four geometries with a single sublattice
 87 coincidence per cell and an angle of twist θ . However it is trivial to demonstrate that the
 88 bilayers resulting from the stacking of $(-q, p + q)_{N,H}$ on the $(q, p)_B$ are related by a simple
 89 inversion and are therefore identical. All this boils down to five hexagonal stackings for the
 90 generic twisted hBN bilayer. It is important to stress that these stacking sequences are not
 91 related to the moiré periodicity and do not impose any constraint on the mutual orientation of
 92 the two layers. The orientation and the stacking are two independent degrees of freedom in the
 93 design of the bilayer structure. As a consequence, we will designate univocally a twisted bilayer
 94 by the notation $STACK(q, p)$ where the $\{p, q\}$ pair relates to the supercell and hence the moiré
 95 periodicity and angles, and $STACK = BBNN, BNNB, BB, BN$ or NN relates to the atoms in the
 96 coincident sites. Images of these stackings, their layer symmetry group and the transformations
 97 to be applied to the upper layer to switch from one stacking to another (swapping of B/N
 98 atoms or translation by $\pm\tau$) are summarized in Figure 2 and Table 1. It is worth recalling that
 99 with our conventions the angles are positive. Their sign comes from the chirality of twisted
 100 bilayers and is defined according to the screw angle separating B-N bonds at the atom-on-atom
 101 coincidence sites of the supercell, as depicted in the insets of the Figure 2.

102 From this analysis, it appears that the five possible stackings of untwisted bilayers (and
 103 bulk) reported in literature [42, 43] are actually special cases of a more general scheme, in
 104 agreement with the fact that the mutual orientation and the stacking sequence are two in-
 105 dependent degrees of freedom. However it is also important to stress that some “special”
 106 structures, typically the untwisted bilayers, have higher symmetries than those reported in
 107 Table 1 and Figure 2.

108 For comparison, in the case of graphene bilayers both B and N labels become C, so the
 109 possible stackings are only two, but they have higher symmetry. The first belongs to the $p321$
 110 layer group and to the odd bilayer graphene (BLG) set [34, 41, 44, 45], has a single sublattice
 111 vertical coincidence per cell and the twist angle is θ . The second belongs to the $p622$ layer
 112 group and to the even BLG set with hexagon-on-hexagon or double sublattice coincidence.
 113 Its rotation angle is $-\theta'$. Finally, if we swap the values of p and q , we will obtain five new
 114 stackings which are the mirror images of the pristine structures. They will have the same
 115 electronic structure, and the twist angles will be $+\theta'$ for the BNNB and BBNN and $-\theta$ for the
 116 BB, BN and NN stackings. Complete definitions and demonstrations are given in Appendices A
 117 to F.

Table 1: The geometry of the five stackings of hBN twisted bilayers. The lower layer is based on the $(q, p)_B$ supercell.

upper layer	twist angle	symm. group	stacking sequence	double coincidence
$(p, q)_B$	$+\theta$	$68(p321)$	BB	no
$(p, q)_N$	$-\theta'$	$68(p321)$	BNNB	yes
$(p, q)_H$	$+\theta$	$68(p321)$	NN	no
$(-q, p + q)_B$	$-\theta'$	$67(p312)$	BBNN	yes
$(-q, p + q)_N$	$+\theta$	$65(p3)$	BN	no
$(-q, p + q)_H$	$+\theta$	$65(p3)$	BN	no

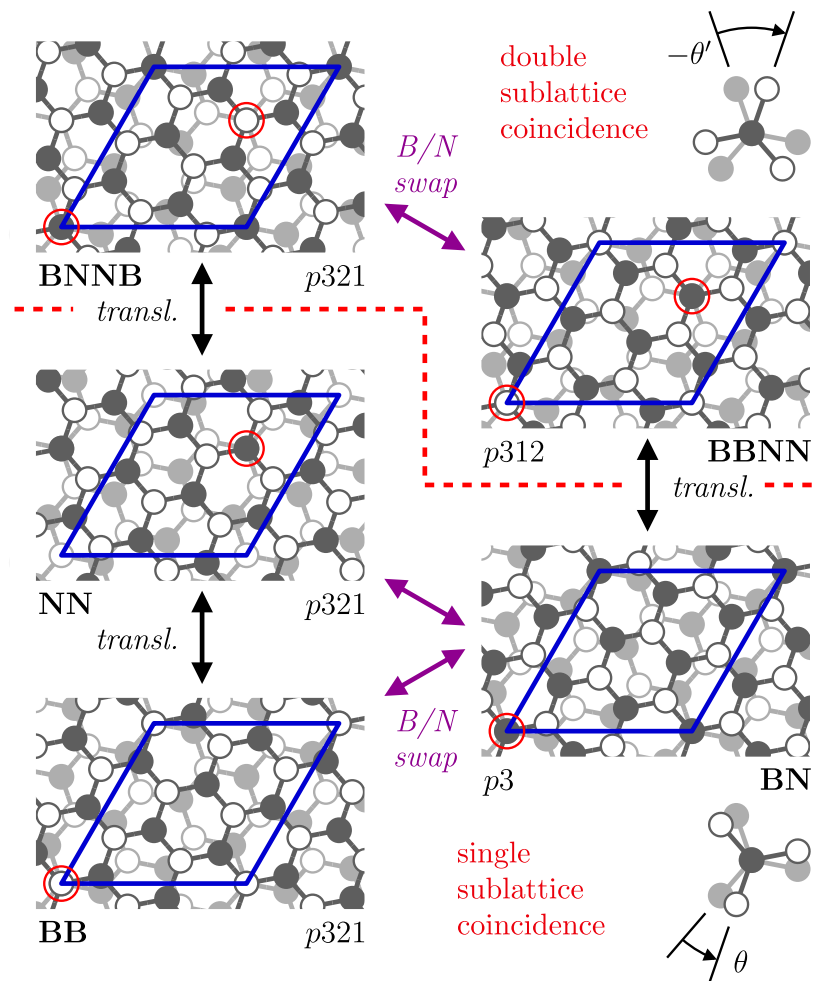


Figure 2: The five stackings of hBN moiré structures, with $p = 2$ and $q = 1$. The sublattice coincidences are highlighted with red circles. The reported symmetry groups are for twisted bilayers (untwisted bilayers have different symmetry properties).

118 Before concluding this part, let us stress once more that the analysis we conducted on hBN
 119 bilayers is very general and easily applicable to any bilayer with hexagonal symmetry such as
 120 dichalcogenide bilayers or BN/graphene heterostructures, for instance.

121 2 Electronic structure

122 Based on our robust symmetry analysis, we clearly identify five different stackings of hBN
 123 bilayers. Zhao and coworkers [33] studied two of them (the NN and the BN one) with a DFT
 124 method based on a tight-binding Hamiltonian and demonstrated that the stacking sequence
 125 has an impact on the spatial localization of the top valence and bottom conduction states.
 126 On the other hand, in a previous work [38] we proved that interlayer coupling, and so the
 127 stacking, is crucial in the formation of the indirect band gap of the bulk phase. These elements
 128 clearly indicate that a complete investigation involving all the stackings is mandatory. As a
 129 consequence, we have performed first-principle simulations with density functional theory
 130 (DFT) to investigate the impact of the stacking sequence on the band gap. We scrutinized
 131 thirty bilayers: six $\{p, q\}$ pairs per each stacking. All the pertinent calculation parameters can
 132 be found in Appendix G.

Table 2: The band splitting (meV) at M and K in the top valence and bottom conduction of the (1,2) supercells. The symbol ‘-’ indicates a band crossing. These features are highlighted with red vertical lines in Figure 3.

Structure	Top valence		Bottom conduction	
	@M	@K	@M	@K
BNNB(1,2)	83	-	25	-
BN(1,2)	61	-	104	-
NN(1,2)	148	20	178	-
BB(1,2)	38	-	232	110
BBNN(1,2)	163	20	273	110

133 As a first step, we investigated the structural stability of the five principal untwisted bilayers
 134 and identified two main groups (see Figure 11 in Appendix H). In the three most stable
 135 structures (BN(0,1), BNNB(0,1) and BB(0,1)) the layers are separated by about 3.1 Å. The
 136 two least stable bilayers (BBNN(0,1) and NN(0,1)) are around 20 meV per formula unit at
 137 higher energy with larger equilibrium interlayer distances (around 3.4 Å). Regarding the elec-
 138 tronic properties, untwisted bilayers with a B-on-B coincidence (BBNN(0,1) and BB(0,1)) have
 139 an indirect band gap whereas the other structures have a direct gap. More details about the
 140 untwisted bilayers can be found in Appendix H.

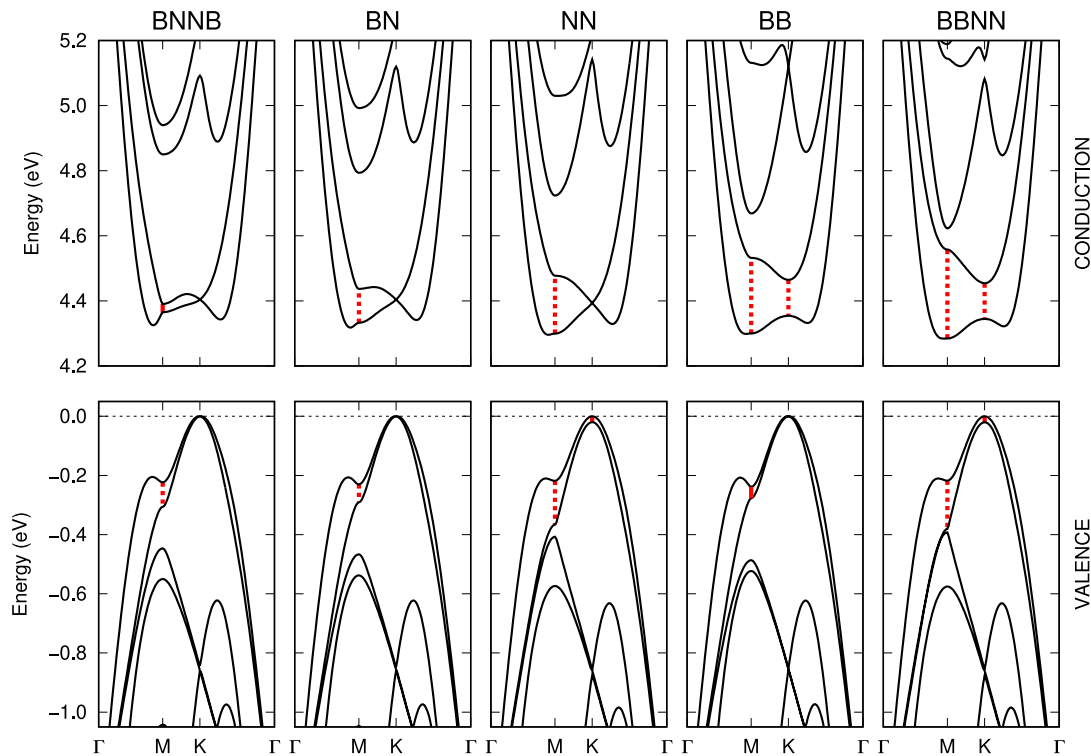


Figure 3: Bottom conduction and top valence of the five principal stackings in the (1,2) supercell. Red vertical dashed lines highlight the notable splittings at M and K reported also in Table 2.

141 We now discuss twisted bilayers. We focus on the (1,2) configuration for all stackings
 142 because notable effects are more distinguishable. The DFT results are reported in Figure 3
 143 inside the Brillouin zone of the supercell. It is important to recall that the preservation of
 144 the hexagonal symmetry of the supercell implies the conservation of their order-3 rotation

Table 3: The DFT energy (eV) of the indirect band gap at different twist angles and stacking sequences. In parenthesis: energy difference between the direct and the indirect band gap in meV.

family	(q, p) cell	BNNB	BN	NN	BB	BBNN
$\delta = 1$	(1,2)	4.325 (71)	4.318 (76)	4.296 (88)	4.299 (55)	4.284 (60)
	(2,3)	4.221 (30)	4.217 (34)	4.211 (38)	4.203 (41)	4.202 (42)
	(3,4)	4.153 (15)	4.153 (16)	4.151 (17)	4.145 (18)	4.146 (19)
	(4,5)	4.102 (5)	4.103 (5)	4.101 (5)	4.098 (5)	4.099 (5)
$\delta = 2$	(1,3)	4.284 (137)	4.284 (137)	4.284 (137)	4.284 (136)	4.284 (136)
	(3,5)	4.240 (72)	4.241 (72)	4.240 (72)	4.240 (72)	4.241 (72)

145 axes without which the equivalence between the K points of the Brillouin zone would be
 146 lost. Interestingly, our calculations reveal that the gap is always indirect irrespective of the
 147 stacking with values around 4.3 eV (see first row of Table 3). Indirect band gap has been
 148 reported also in untwisted bilayers of different stacking [42, 43], hBN multilayers [31], and
 149 bulk phases of different stackings [38, 42], indicating that this is indeed a robust characteristic
 150 of BN multilayers. By analyzing in details the electronic structure, we can distinguish the
 151 stackings according to characteristics at the K and M points. In the valence region we observe
 152 that when N atoms are on top of each other (the NN and the BBNN stackings), a band crossing
 153 is avoided in the top valence at K while the splitting between the HOMO and HOMO-1 at M
 154 is the largest. On the conduction band, the splitting between the LUMO and the LUMO+1
 155 at M is reduced along the sequence BBNN, BB, NN, BN and BNNB while the presence of B
 156 atoms on top of each other (BB and BBNN stackings) prevents a band crossing at K . All the
 157 features discussed here are highlighted with dashed vertical red lines in Figure 3 and reported
 158 in Table 2. We expect these effects to be less important at extremal twist angles (i.e. close to
 159 0° and 60°) because the immediate surroundings of each atom change progressively.

160 Let us now discuss the evolution of the band gap as a function of the twist angle. In Table 3
 161 and in Figure 4 we summarize our DFT results on the indirect band gap and the difference
 162 between direct and indirect gap. First, we observe that the gapwidth gets smaller (higher) for
 163 smaller θ (θ'), demonstrating a trend opposite to what predicted by continuous models [32].
 164 Typically, for θ varying from 21.79° to 7.34° , the gap decreases by about 5%. Secondly we
 165 observe that in each stacking the gap remains indirect at all angles. This finding contrasts
 166 with density-functional tight-binding results where direct gaps at all twist angles are obtained
 167 instead [33]. A possible explanation of this discrepancy resides in a bad accounting of the
 168 interlayer interactions. In fact, our study of the exciton dispersion [38] demonstrates that
 169 the interlayer hopping terms are of paramount importance for the formation of the indirect
 170 band gap. A more detailed analysis reported in Appendix I allows us to affirm that it is not an
 171 artifact coming from σ or nearly-free-electron states located at higher energies [15, 46–51].
 172 We should stress that these results are reliable as long as one considers energy differences and
 173 trends, absolute gap energies being systematically underestimated by DFT. Indeed, we expect
 174 hybrid potential calculations or quasiparticle corrections included via the GW approximation
 175 to be almost identical from one system to the other, and to have minor effect on the dispersion
 176 of s and p states [15, 31]. We are confident on this because of the successful use of the scissor
 177 operator in BN compounds [16, 38, 39] and direct comparisons between different methods [16,
 178 31, 37, 42, 52].

179 We can now pass to the investigation of the evolution of the full band structure as a function
 180 of the twist angle. In the main text we discuss two paradigmatic stackings, the BN and the
 181 NN and we report the corresponding twelve band structure plots in Figure 5. We refer the
 182 reader to the Appendix K and Figure 15 for the other bandplots. We observe that conduction

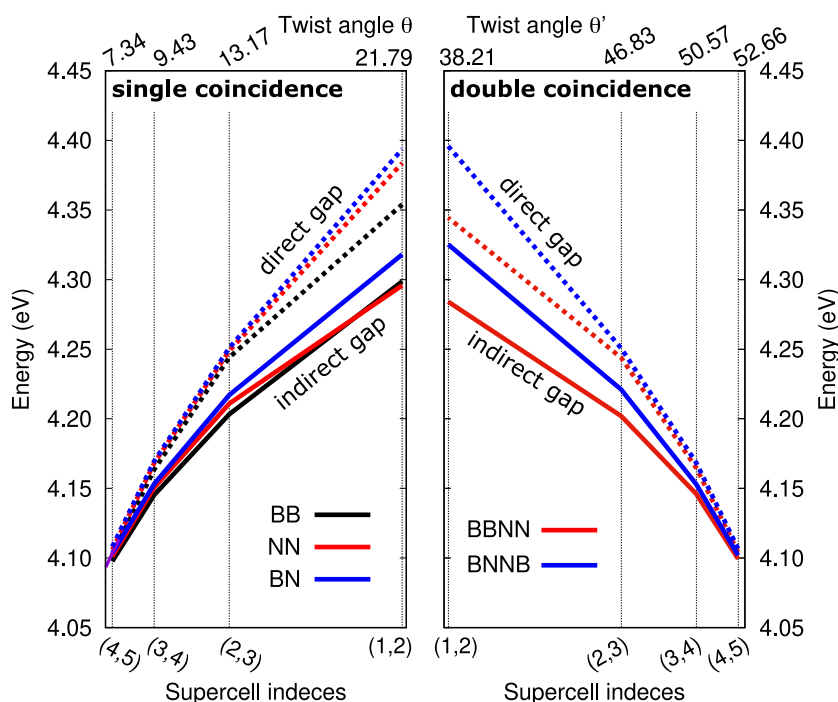


Figure 4: Indirect gap (solid lines) and direct gap (dashed lines) of the five stackings as a function of the twist angle (θ or θ' depending on the stacking) within the $\delta = 1$ family.

183 and valence bands get flatter at smaller θ (and larger θ') as highlighted in Figure 5. This
 184 implies the progressive creation of localized valence and conduction states in agreement with
 185 what shown by Zhao and coworkers [33]. For example, in the BN stacking at $\theta = 7.34^\circ$,
 186 the HOMO and LUMO states are characterized by bandwidths around 0.09 eV and 0.16 eV,
 187 respectively. Flatter bands are not observed since this would demand much smaller angles
 188 which are inaccessible with our numerical resources. Because of the flattening of the bands,
 189 it is possible to tune the difference between indirect and direct gap through the twist angle,
 190 and so possibly to convert progressively the radiative decay pathway from a phonon-assisted
 191 emission to a direct recombination. This may have strong impact on the intensity of emitted
 192 light (probability of recombination), its temperature dependence (through the coupling with
 193 phonons) and finally the life time of excitations.

194 In addition we observe that $\{p, q\}$ pairs can be grouped into families defined by the param-
 195 eter $\delta = |p - q|$ that characterizes the interplay between crystalline structure (twist angle) and
 196 electronic structure (bands). In fact, the bands around the gap within the same family look
 197 similar but shrunk and flattened at small θ (or larger θ'). Once more, the case δ multiple of 3
 198 shall be excluded. Consider the family $\delta = 1$, corresponding to the first four plots from the left
 199 in the band plots of Figure 5. Here the valence bands present a maximum in K and are formed
 200 of two bands dispersing almost parabolically, up to M where one of the two deviates with a
 201 small bump. In conduction, two valleys are well discernible between K and Γ and around
 202 M , the latter forming the conduction band minimum. Formally, the untwisted bilayers fall in
 203 this very family. However, their band structure presents unique characteristics and thus differs
 204 from that of the twisted counterparts (cfr the untwisted band structures reported in [42]). At
 205 the time being, we can not identify the reason for this deviation, but we hypothesize that it
 206 is due to the fact that untwisted bilayers have higher symmetries than the twisted bilayers of
 207 the same stacking. Because of this unicity, we have not added the untwisted band structures
 208 to the bandplots of Figures 5 and 15.

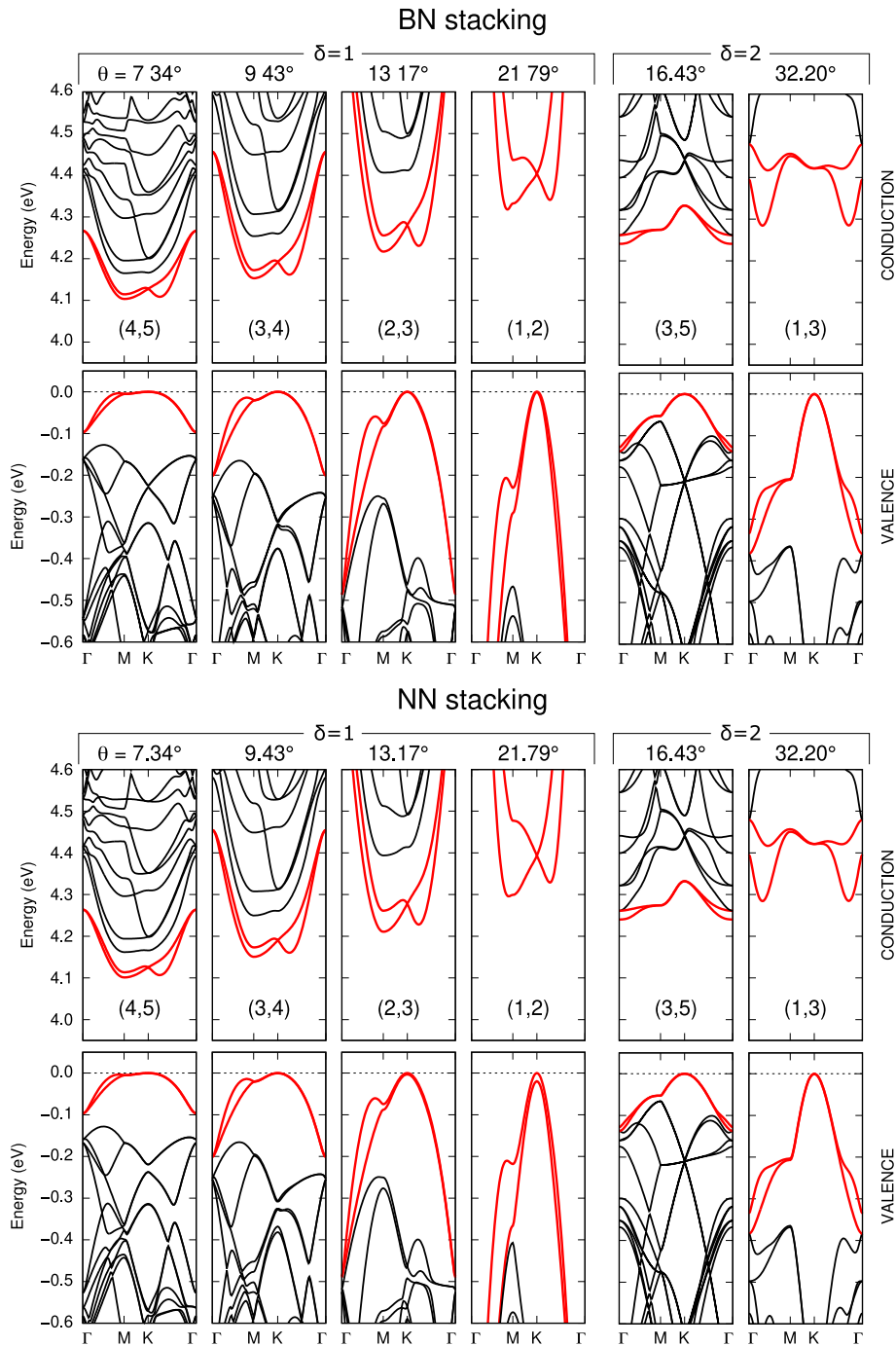


Figure 5: Bottom conduction and top valence of the BN (top panel) and NN (bottom panel) stackings at different twist angles.

209 The last two plots from the left in the band plots of Figure 5 belong to the $\delta = 2$ family.
 210 These bandplots look very different from those of the other family, even though the gap remains
 211 indirect with the top valence at K . As before, one can see common features within this family
 212 despite the band shrinking. The valence band has a characteristic double-dome shape (with
 213 a dome on top of another) and a maximum in K . In the conduction band, the two bottom
 214 bands almost coincide in the $M - K$ path and present two minima close to or at Γ . We verified
 215 that the bottom conduction in the $\delta = 2$ family does fall in the $\Gamma - M$ high symmetry line (see
 216 Appendix J).

217 3 Conclusions

218 To conclude, we have demonstrated that in hBN bilayers there are five stackings that are in-
 219 variant under rotations of 120° like the pristine hBN monolayers. We have listed the symmetry
 220 groups of these stackings, shown how to construct them and how to transform one into another
 221 and we have introduced a physically informative nomenclature allowing to identify them un-
 222 ambiguously. We also have provided a precise definition of the twist angle (θ or θ' depending
 223 on the stacking). All this contrasts with graphene bilayers, where only two stackings can be de-
 224 fined. Our nomenclature is completely general and can be applied to any homobilayer formed
 225 of hexagonal 2D materials (twisted as well as untwisted). Even though corrugation and do-
 226 main relaxation have to be expected in experimental realization of these systems [30, 53–55],
 227 these structural modifications will still be constrained by the stacking sequence. By performing
 228 DFT simulations, we have done a thorough study of the electronic structure of hBN bilayers
 229 taking into account both its dependence on the stacking sequence and the twist angle. In
 230 the first case, we have traced a correlation between the atom-on-atom coincidences and some
 231 characteristics of the states which form the gap. In the second case, we have shown that the
 232 gapwidth is always indirect irrespective of the twist angle and it decreases for decreasing θ or
 233 for increasing θ' , differently from what previously predicted on the basis of less sophisticated
 234 simulation schemes [32]. Finally we have identified the structural parameter $\delta = |p - q|$ which
 235 allows to classify bilayers into families with similar band structures. The stacking- and angle-
 236 dependent properties discussed in this letter have special importance in possible twistrionic
 237 applications. In fact these mechanisms are expected to have a strong impact on the optical
 238 properties of these bilayers and in particular on the direct manipulation of interlayer excitons
 239 which can be stabilized through the application of an external field.

240 Acknowledgments

241 The authors are thankful to Dr. F. Paleari for fruitful discussions and the dedicated analysis
 242 tools he provided. They also acknowledge the contribution of F. Ducastelle who seeded this
 243 work. Finally, they acknowledge funding from the European Union’s Horizon 2020 research
 244 and innovation program under grand agreement N° 881603 (Graphene Flagship core 3) and
 245 from the French National Agency for Research (ANR) under the projects EXCIPLINT (Grant
 246 No. ANR-21-CE09-0016).

247 A Asymmetric honeycomb supercells

248 As presented in the main article, we choose the two primitive vectors of the boron nitride
 249 monolayer \mathbf{a}_1 and \mathbf{a}_2 forming an angle of 60° and define the three vectors separating the
 250 nitrogen and the boron sublattices like:

$$\boldsymbol{\tau}_1 = +\mathbf{a}_1/3 + \mathbf{a}_2/3, \quad \boldsymbol{\tau}_2 = \boldsymbol{\tau}_1 - \mathbf{a}_1, \quad \boldsymbol{\tau}_3 = \boldsymbol{\tau}_1 - \mathbf{a}_2.$$

251 A boron atom is located at the origin of the honeycomb and nitrogen is located at $\boldsymbol{\tau}_1$. A new
 252 periodic super-lattice is constructed with the new translational vectors \mathbf{A}_1 and \mathbf{A}_2 written on
 253 the basis $\{\mathbf{a}_1, \mathbf{a}_2\}$ like

$$\mathbf{A}_i = \sum_j M_{ij} \mathbf{a}_j. \quad (\text{A.1})$$

254 In the bilayer system, the hexagonal supercell for the lower layer has been arbitrarily chosen
 255 as the one produced by the matrix

$$M^{(q,p)} = \begin{bmatrix} q & p \\ -p & p+q \end{bmatrix}, \quad (\text{A.2})$$

256 and the upper layer is developed either with

$$M^{(p,q)} = \begin{bmatrix} p & q \\ -q & p+q \end{bmatrix}, \quad (\text{A.3})$$

257 or with

$$M^{(-q,p+q)} = \begin{bmatrix} -q & p+q \\ -p-q & p \end{bmatrix}. \quad (\text{A.4})$$

258 In all these cases, p and q are integers. The vertical mirror planes along the $[11]$ and $[10]$
 259 directions of the supercell are lost only if

$$p \neq 0, q \neq 0 \text{ and } p \neq q,$$

260 then, we call such supercell *asymmetric*. These are the supercells considered in this work
 261 because they lead to twisted bilayers.

262 Lastly, the $\{p, q\}$ integers define also the parameter length, the surface Ω and the number
 263 of atoms N_{at} of the three supercells

$$|A_i| = a\sqrt{p^2 + q^2 + pq}, \quad (\text{A.5})$$

$$\Omega = \Omega_0(p^2 + q^2 + pq), \quad (\text{A.6})$$

$$N_{\text{at}} = 2(p^2 + q^2 + pq), \quad (\text{A.7})$$

264 where $\Omega_0 = \frac{a^2\sqrt{3}}{2}$ is the surface, and a is the cell parameter of the honeycomb primitive cell.

265 As we mention in the main article, the origin of a generic (k, s) supercell can be set either
 266 on an atom or on the center of a hexagon of the underlying honeycomb lattice. We want to
 267 analyze what happens at the direct-space high-symmetry points (00) , $(\frac{1}{3}, \frac{1}{3})$ and $(\frac{2}{3}, \frac{2}{3})$ of the
 268 supercell where the axes of order-3 rotation symmetry pass (cfr. below). These points are
 269 highlighted with red dots in Figure 1 of the main article. Using (A.3) we write

$$\begin{pmatrix} X & X \\ 3 & 3 \end{pmatrix} = \frac{X}{3}\mathbf{A}_1 + \frac{X}{3}\mathbf{A}_2 \quad (\text{A.8})$$

$$= \frac{X}{3}(k-s)\mathbf{a}_1 + \frac{X}{3}(k+2s)\mathbf{a}_2, \quad (\text{A.9})$$

270 where the integer $X = 1$ or 2 selects the supercell high symmetry point. Let us introduce now
 271 the integer parameter α defined as

$$k-s = 3t + \alpha,$$

272 with $t \in \mathbb{Z}$, so only $-1, 0$ and 1 are meaningful values of α . Using it in equation (A.9), we get

$$\begin{pmatrix} X & X \\ 3 & 3 \end{pmatrix} = \frac{X}{3}(3t + \alpha)\mathbf{a}_1 + \frac{X}{3}(3t + 3s + \alpha)\mathbf{a}_2 \quad (\text{A.10})$$

$$= \underbrace{Xt\mathbf{a}_1 + X(t+s)\mathbf{a}_2}_{=\mathbf{R}} + \frac{X\alpha}{3}(\mathbf{a}_1 + \mathbf{a}_2), \quad (\text{A.11})$$

Table 4: Determination of the kind of the sublattices located at the high symmetry points used in our construction of bilayers for a generic $\{p, q\}$ pair, and the name of the resulting bilayer.

supercell	α	(00)	$(\frac{1}{3} \frac{1}{3})$	$(\frac{2}{3} \frac{2}{3})$	α	(00)	$(\frac{1}{3} \frac{1}{3})$	$(\frac{2}{3} \frac{2}{3})$	name of the bilayer obtained
$(q, p)_B$	-1	B	H	N	+1	B	N	H	by stacking on the $(q, p)_B$
$(p, q)_B$		B	N	H		B	H	N	BB(q, p)
$(p, q)_N$	+1	N	H	B	-1	N	B	H	BNNB(q, p)
$(p, q)_H$		H	B	N		H	N	B	NN(q, p)
$(-q, p + q)_B$		B	H	N		B	N	H	BBNN(q, p)
$(-q, p + q)_N$	-1	N	B	H	+1	N	H	B	BN(q, p)
$(-q, p + q)_H$		H	N	B		H	B	N	BN(q, p)

where \mathbf{R} is a honeycomb lattice vector. Therefore, if $\alpha = -1$ and $X = 1$, the site located in $(\frac{1}{3} \frac{1}{3})$ of the *supercell* will coincide with the site located at $(-\frac{1}{3} -\frac{1}{3}) = (\frac{2}{3} \frac{2}{3})$ of the *primitive cell* of the honeycomb lattice, and vice-versa if $X = 2$. But if $\alpha = +1$, the site in $(\frac{1}{3} \frac{1}{3})$ will coincide with the site in $(\frac{1}{3} \frac{1}{3})$ of the primitive cell, and the same for $X = 2$. Actually, we demonstrate below in Appendix D that the case $\alpha = 0$ is irrelevant.

Lastly, it is easy to demonstrate that if a given supercell (p, q) has a $\alpha = +1$ parameter, then the supercells (q, p) and $(-q, p + q)$ have a $\alpha = -1$ parameter (and inversely).

B Stacking geometries

As we mentioned in the main article, our construction of the moiré geometries requires two integers $\{p, q\}$ and follows the rules: (i) the lower layer is always defined by the $(q, p)_B$ supercell (origin at boron) and (ii) the upper layer is either defined by the $(p, q)_X$ cell or the $(-q, p + q)_X$ cell, where X labels the origin of the supercell (B = boron, N = nitrogen, H = hexagon center). As shown in the previous section, the (p, q) -on- (q, p) constructions will always be made of supercells with opposite α parameters, whereas the $(-q, p + q)$ -on- (q, p) constructions will always result from supercells with the same α . The Table 4 lists the kind of sublattice (boron atom, nitrogen atom, or hexagon center) that occurs at the high symmetry points for both values of α of the lower layer $(q, p)_B$.

For any choice of p and q , the six possible stackings are:

1. The $(p, q)_B$ -on- $(q, p)_B$ is a single coincidence structure, with B-on-B at the origin, N-on-hexagon at one of the two high-symmetry points and a hexagon-on-N at the other one. There is no hexagon-on-hexagon vertical alignment for the single coincidence structures. We call this structure the BB(q, p) bilayer.
2. The $(p, q)_N$ -on- $(q, p)_B$ is a double coincidence structure, with N-on-B at the origin, B-on-N at one of the two high-symmetry points and an hexagon-on-hexagon at the other one. We call it the BNNB(q, p) bilayer.
3. The $(p, q)_H$ -on- $(q, p)_B$ is again a single coincidence structure, with a hexagon-on-B at the origin, B-on-hexagon at one of the two high-symmetry points and an N-on-N at the other one. We call it the NN(q, p) bilayer.
4. The $(-q, p + q)_B$ -on- $(q, p)_B$ is another double coincidence structure, with B-on-B at the origin, N-on-N at one of the two high-symmetry points and an hexagon-on-hexagon at the other one. We call it the BBNN(q, p) bilayer.

- 304 5. The $(-q, p + q)_{\text{N-on}}-(q, p)_{\text{B}}$ is a single coincidence structure, with N-on-B at the origin,
 305 N-on-hexagon at one of the two high-symmetry points and an B-on-hexagon at the other
 306 one. We call it the $\text{BN}(q, p)$ bilayer.
- 307 6. The $(-q, p + q)_{\text{H-on}}-(q, p)_{\text{B}}$ is a single coincidence structure, with a hexagon-on-B at the
 308 origin, N-on-hexagon at one of the two high-symmetry points and an B-on-N at the other
 309 one. It is the same geometry than the $\text{BN}(q, p)$ above.
- 310 Finally, since the stacking 6 leads actually to the same structure as stacking 5, for each $\{p, q\}$
 311 pair of integer we construct five and only five different structures that preserve the atom-on-
 312 atom vertical alignments.

313 C Moiré stacking angles

314 The easiest way to derive the twist angle between two bilayers is by representing the vectors of
 315 the honeycomb lattice with discrete complex numbers. Here, we adopt the notation [41, 45]
 316 $\mathcal{Z}(m, n) = mz_1 + nz_2$ with $z_1 = 1$ and $z_2 = \frac{1}{2} + \frac{\sqrt{3}}{2}i$. The angles are just the arguments calculated
 317 like

$$\exp(i\theta) = \frac{\mathcal{Z}(q, p)}{\mathcal{Z}(p, q)}, \quad (\text{C.1})$$

$$\exp(i\theta') = \frac{\mathcal{Z}(-q, p + q)}{\mathcal{Z}(q, p)}, \quad (\text{C.2})$$

318 and depend only on the $\{p, q\}$ pair of integers. This leads to

$$\tan \theta_{\{p, q\}} = \sqrt{3} \frac{p^2 - q^2}{p^2 + q^2 + 4pq}, \quad (\text{C.3})$$

$$\tan \theta'_{\{p, q\}} = \sqrt{3} \frac{q^2 + 2pq}{2p^2 - q^2 + 2pq}, \quad (\text{C.4})$$

319 which are given in the main article. Since the p and q indices can take any integer value, the
 320 angles are always defined modulo 60° . The constructed supercells and the resulting angles θ
 321 and θ' are drawn in Figure 6.a.

322 So far, the vectors defined by (A.1) have been developed on the $\{\mathbf{a}_1, \mathbf{a}_2\}$ honeycomb lattice
 323 basis, but we could have chosen either to develop them on the $\{\mathbf{a}_2 - \mathbf{a}_1, -\mathbf{a}_1\}$ basis and then
 324 work with the $\{-p - q, p\}$ pair, or on the $\{-\mathbf{a}_2, \mathbf{a}_1 - \mathbf{a}_2\}$ basis, and work with the $\{q, -p - q\}$ pair.
 325 So, definitions (C.3) and (C.4) are not unique and the angles could have also been defined as

$$\tan \theta_{\{-p - q, p\}} = \sqrt{3} \frac{q^2 + 2pq}{-2p^2 + q^2 - 2pq}, \quad (\text{C.5})$$

$$\tan \theta'_{\{-p - q, p\}} = \sqrt{3} \frac{-p^2 - 2pq}{-p^2 + 2q^2 + 2pq}, \quad (\text{C.6})$$

326 or

$$\tan \theta_{\{q, -p - q\}} = \sqrt{3} \frac{p^2 + 2pq}{-p^2 + 2q^2 + 2pq}, \quad (\text{C.7})$$

$$\tan \theta'_{\{q, -p - q\}} = \sqrt{3} \frac{-p^2 + q^2}{p^2 + q^2 + 4pq}, \quad (\text{C.8})$$

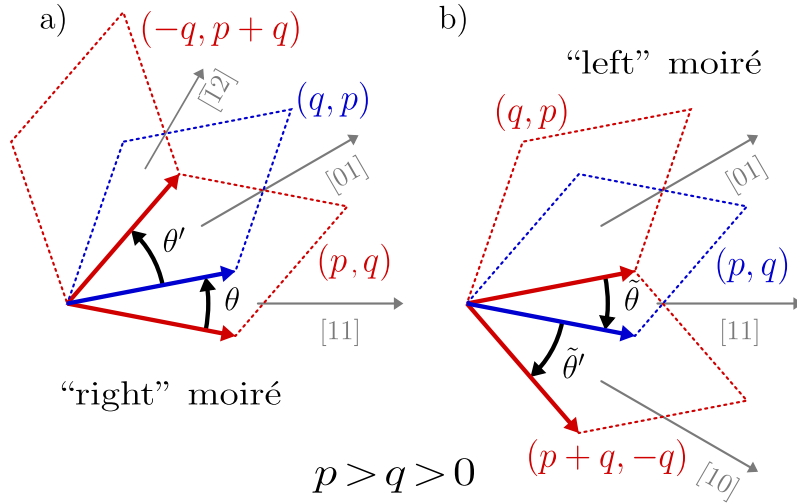


Figure 6: a) The angles θ and θ' , based on the (q, p) geometries (that are used in the main article). b) The angles $\tilde{\theta}$ and $\tilde{\theta}'$ corresponding to the mirror images of the previous ones. They are based on the (p, q) geometries.

327 which are also valid formulations. It is trivial to show that for any θ of equations (C.3), (C.5),
 328 or (C.7) and for any θ' of equations (C.4), (C.6), or (C.8), the following equality

$$\theta' = -\theta + \frac{n\pi}{3},$$

329 holds for an integer $n \in \mathbb{Z}$. In order to avoid confusion and give a non ambiguous definitions of
 330 our moiré structures, we decide arbitrarily to adopt definitions (C.3) and (C.4), and to impose

$$p > q > 0.$$

331 In this situation, the vectors $p\mathbf{a}_1 + q\mathbf{a}_2$ and $q\mathbf{a}_1 + p\mathbf{a}_2$ lie in the $\{\mathbf{a}_1, \mathbf{a}_2\}$ angular sector, and the
 332 vector $-q\mathbf{a}_1 + (p+q)\mathbf{a}_2$ lie in the $\{\mathbf{a}_2, \mathbf{a}_2 - \mathbf{a}_1\}$ angular sector. As a consequence

$$\theta, \theta' \in \left]0, \frac{\pi}{3}\right[\quad \text{and} \quad \theta + \theta' = \frac{\pi}{3},$$

333 implying that $\text{BB}(q, p)$, $\text{BN}(q, p)$ et $\text{NN}(q, p)$ have an angle $+\theta > 0$ and $\text{BBNN}(q, p)$, $\text{BNNB}(q, p)$
 334 have an angle $-\theta' < 0$. These five stackings are chiral structures, that we decide to name
 335 “right-hand” moiré bilayers.

336 To construct the enantiomers of the “right-hand” moiré bilayers above, we have to trans-
 337 form the vectors \mathbf{A}_1 defining the hexagonal supercells (A.1). They are mirrored respect the
 338 $[11]$ crystallographic direction of the primitive honeycomb lattice cell, as shown in the Fig-
 339 ure 6.b. The lower layer of a “left” moiré is now carried by the supercell $M^{(p,q)}$ and the upper
 340 layer is developed either on the $M^{(q,p)}$ or the $M^{(p+q,-q)}$ one, still within the constraint $p > q > 0$.
 341 The corresponding twist angles are now

$$\exp(i\tilde{\theta}) = \frac{\mathcal{Z}(p, q)}{\mathcal{Z}(q, p)}, \tag{C.9}$$

$$\exp(i\tilde{\theta}') = \frac{\mathcal{Z}(p+q, -q)}{\mathcal{Z}(p, q)}, \tag{C.10}$$

342 leading to $\tilde{\theta} = -\theta$ and $\tilde{\theta}' = -\theta'$ then

$$\tilde{\theta}, \tilde{\theta}' \in \left]-\frac{\pi}{3}, 0\right[\quad \text{and} \quad \tilde{\theta} + \tilde{\theta}' = -\frac{\pi}{3}.$$

343 As a result, the “left” $BB(p, q)$, $BN(p, q)$ and $NN(p, q)$ have an angle $-\theta < 0$, and the “left”
 344 $BBNN(p, q)$ and $BNNB(p, q)$ have an angle $+\theta' > 0$.

345 In absence of any magnetic field, the “right-hand” and “left-hand” corresponding stackings
 346 exhibit exactly the same electronic properties. That is why we restricted our study to the
 347 “right-hand” ones.

348 **D Redundancy of the case $(p - q = 3t)$**

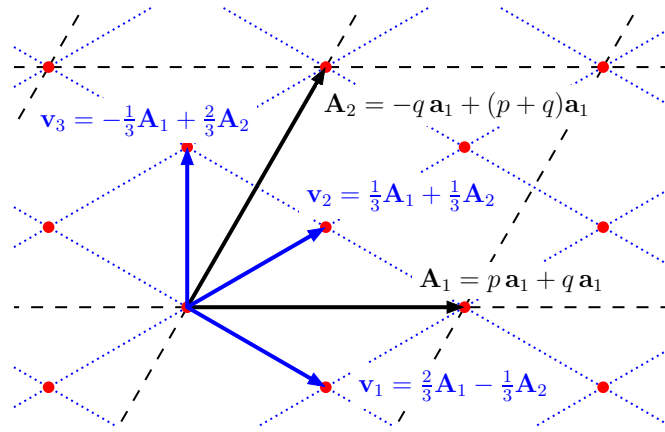


Figure 7: The upper layer asymmetric supercell (p, q) with $p = q + 3t$. It is always possible to construct a smaller supercell since \mathbf{v}_1 , \mathbf{v}_2 and \mathbf{v}_3 are vectors of the honeycomb lattice. In other words, the twisted bilayer geometries constructed from the $(q, q + 3t)$ supercell are not primitive cells of the moiré.

349 The case $\alpha = 0$ corresponds to moiré (p, q) supercells where $p - q = 3t$ and t is an integer.
 350 So

$$\begin{bmatrix} q + 3t & q \\ -q & 2q + 3t \end{bmatrix} = (q + 3t, q) \text{ supercell.} \quad (\text{D.1})$$

351 As we sketched in Figure 7, starting from the vectors \mathbf{A}_1 and \mathbf{A}_2 , we can define new shorter
 352 vectors

$$\mathbf{v}_1 = \frac{2}{3}\mathbf{A}_1 - \frac{1}{3}\mathbf{A}_2 = (q + 2t)\mathbf{a}_1 - t\mathbf{a}_2, \quad (\text{D.2})$$

$$\mathbf{v}_2 = \frac{1}{3}\mathbf{A}_1 + \frac{1}{3}\mathbf{A}_2 = t\mathbf{a}_1 + (q + t)\mathbf{a}_2, \quad (\text{D.3})$$

$$\mathbf{v}_3 = -\frac{1}{3}\mathbf{A}_1 + \frac{2}{3}\mathbf{A}_2 = (-q - t)\mathbf{a}_1 + (q + 2t)\mathbf{a}_2, \quad (\text{D.4})$$

353 and since q and t are integers, the vectors \mathbf{v}_i are honeycomb bravais lattice vectors. In this
 354 situation, the supercell defined by the indices of the vector \mathbf{v}_3 (for example) is

$$\begin{bmatrix} -q - t & q + 2t \\ -q - 2t & t \end{bmatrix} = (-q - t, q + 2t) \text{ supercell,} \quad (\text{D.5})$$

355 which is also an asymmetric hexagonal supercell, three times smaller than the original $(q + 3t, q)$
 356 one.

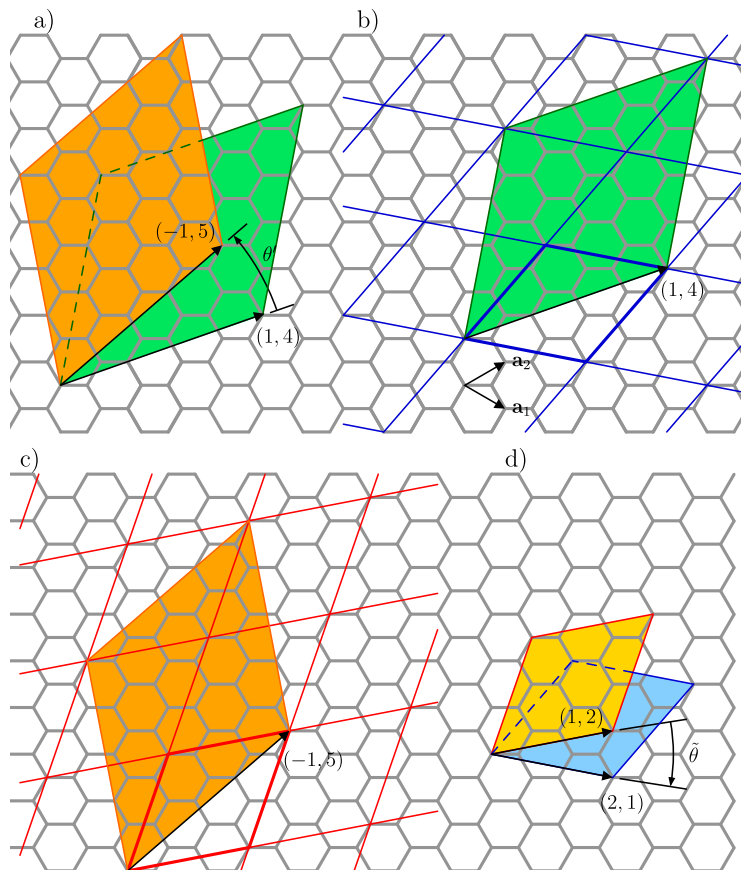


Figure 8: a) Construction of the moiré bilayer based on the (1,4) supercell for the lower layer and the (-1,5) for the upper layer. b) The lower supercell can be tessellated by the (2,1) smaller supercell. c) The upper one is also a tessellation of the (1,2) supercell. d) The angle of the “left-hand” small moiré is the same as that of the large non-primitive moiré $\hat{\theta}_{\{2,1\}} = -\theta'_{\{1,4\}}$.

357 Moreover, the twist angles (C.3) calculated with p and q indices (when $p = q + 3t$) are

$$\tan \theta_{\{q+3t,q\}} = \sqrt{3} \frac{3t^2 + 2qt}{2q^2 + 3t^2 + 6qt},$$

$$\tan \theta'_{\{q+3t,q\}} = \sqrt{3} \frac{q^2 + 2qt}{q^2 + 6t^2 + 6qt},$$

358 and it is straightforward to verify than these two tangents are exactly the same if we calculate
 359 them with the $-q - t$ and $q + 2t$ indices.

360 To summarize, (i) the $\{q + 3t, q\}$ set leads to non primitive moiré supercells, and (ii) it is
 361 always possible to use the $\{-q - t, q + 2t\}$ pair which gives the same twist angles but in three
 362 times smaller supercells. As an illustration of it, in Figure 8 we have drawn the example of the
 363 construction of the (-1,5)-on-(1,4) moiré and its reduction to the (1,2)-on-(2,1) “left-hand”
 364 moiré bilayer.

365 E Completeness of the description with (q, p) pairs

366 In this section we show that all possible hexagonal supercells can be expressed by an appro-
 367 priate choice of the (q, p) pair of integers.

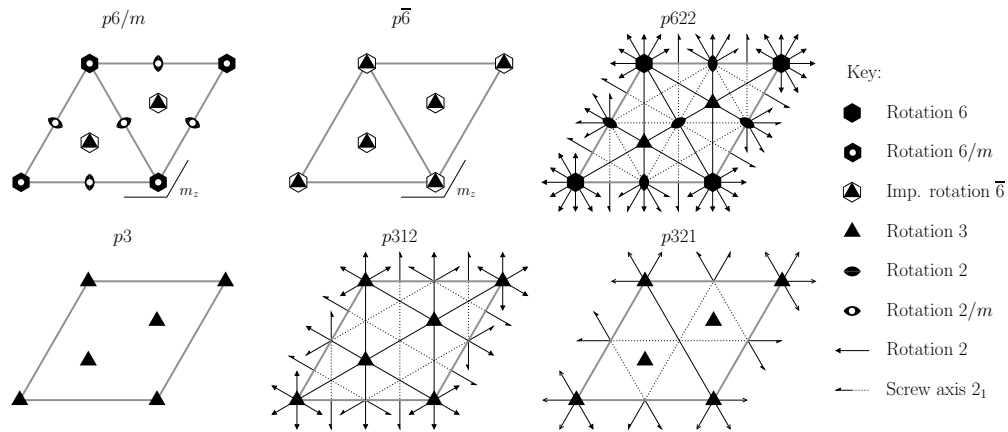


Figure 9: The graphene and hBN moiré bilayers belong to one of these layer groups (adapted from [56]). The trivial group $p1$ is not shown.

368 Let us first highlight the relation between the (q, p) pair and the translational symmetry
 369 of the bilayer. The bottom layer is generated by the two vectors \mathbf{a}_1 and \mathbf{a}_2 spanning an angle of 60° .
 370 On top of it, another hexagonal layer is rotated by some angle around a pivotal point which is placed at the origin of the axes for sake of simplicity. Its primitive vectors are
 371 $\mathbf{c}_1 = \mathcal{R}\mathbf{a}_1$ and $\mathbf{c}_2 = \mathcal{R}\mathbf{a}_2$ defined through the rotation matrix \mathcal{R} . If the resulting structure
 372 has translational symmetry, there must be replicas of the pivotal point and they must form a
 373 supercrystal generated by a unitary supercell with hexagonal symmetry. By definition, it must
 374 be possible to express the unitary supercell as an integer linear combination of the unitary
 375 vectors of each layer. Let it be $\mathbf{A} = q\mathbf{a}_1 + p\mathbf{a}_2$ if expressed in the lower layer unitary vectors,
 376 then it coincides either to $\mathbf{C} = p\mathbf{c}_1 + q\mathbf{c}_2$ or to $\mathbf{C} = -q\mathbf{c}_1 + (p + q)\mathbf{c}_2$ in the the upper layer,
 377 depending on whether it is rotated by θ or θ' , as explained in the previous appendices.
 378

379 In the main text we limited our study to “right-hand” bilayers for which $p > q > 0$, and
 380 twist angles are $+\theta$ and $-\theta'$. These two angles are defined inside the open interval $]0^\circ, 60^\circ[$
 381 and their tangents are comprised in the interval $]0, \sqrt{3}[$. Let us introduce the real number
 382 $\xi \in]0, 1[$. Formulae (C.3) and (C.4) can be expressed in terms of this quantity

$$\tan \theta = \sqrt{3} \frac{1 - \xi^2 - 1}{\xi^2 + 4\xi + 1}, \tag{E.1}$$

$$\tan \theta' = \sqrt{3} \frac{\xi^2 + 2\xi}{-\xi^2 + 2\xi + 2}. \tag{E.2}$$

383 These two expressions are bijective relations mapping $]0, 1[$ to $]0, \sqrt{3}[$. Therefore, one can in-
 384 vert these relations and since the tangent is also invertible, it is possible to establish a bijection
 385 $]0^\circ, 60^\circ[\rightarrow]0, 1[$ mapping any θ or θ' angle to ξ . If ξ is rational, one can always find a pair
 386 of integers (q, p) such that $\xi = q/p$. On the other hand, if it is not rational, then it will not be
 387 possible to find any pair of integers (q, p) corresponding to the chosen angle, but in this case
 388 the system will have no translation symmetry.

389 F Layer groups of moiré structures

390 In Figure 9, we report graphical representations of the symmetries of the layer group used in
 391 this Appendix. The layer group of a graphene monolayer asymmetric supercell is the $p6/m$,
 392 neglecting translations occurring inside the defined cell. For a boron nitride (or a transition
 393 metal dichalcogenide) supercell, the layer group is $p\bar{6}$ [56]. Both groups contain order-3 or

394 order-6 rotations axis along z , located at the high symmetry points of the cell: (00) , $(\frac{1}{3} \frac{1}{3})$
395 and $(\frac{2}{3} \frac{2}{3})$. When stacking two supercells like described in the previous sections, these axes
396 are coincident, and the rotations are always preserved. Thus the 2D crystal systems remain
397 hexagonal.

398 By looking at Table 4 and by replacing all occurrences of B and N by C, it is easy to derive all
399 the stackings of graphene bilayers, however the result is highly redundant. Actually, by taking
400 the origin of all the supercells only on the site corresponding to B atoms in hBN, it is possible to
401 sort out identical geometries from the beginning. In this case, the $(-q, p+q)$ -on- (q, p) structure
402 geometry always shows one “hexagon-on-hexagon” vertical alignment with an order-6 rotation
403 axis, and two atom-on-atom vertical alignments with order-3 rotation axes (*double* sublattice
404 coincidence). The resulting layer group is the hexagonal $p622$, that also contains many in-
405 plane order-2 rotations, oriented along $[10]$ and $[11]$ crystallographic directions as well as
406 many 2_1 screw axes. Note that to comply with the definitions of layer group as defined in
407 Figure 9, the supercell must have the “hexagon-on-hexagon” axis is located at the origin. This
408 means that supercells constructed as we have done in our work must be translated accordingly.
409 Differently, the case of (p, q) -on- (q, p) structure exhibits two “hexagon-on-atom” alignments
410 and one “atom-on-atom” alignment (*single* sublattice coincidence) in the points where order-
411 3 rotation axes pass. If the structure is constructed like proposed above in Appendix B, this
412 “atom-on-atom” coincidence is correctly located at the origin. It is worth noticing that there are
413 in-plane order-2 rotations axes, oriented along the $[10]$ crystallographic directions, passing
414 through the origin. The symmetry group is $p321$ for this case.

415 Let now analyze the symmetry of the hBN moiré bilayers. As explained in the previous
416 sections, the three stackings $BB(q, p)$, $NN(q, p)$, and $BN(q, p)$ correspond geometrically to the
417 graphene bilayer with *single* sublattice coincidence. Note that, as previously, the NN stacking
418 must be translated in such a way that the “atom-on-atom” vertical coincidence is placed at the
419 origin, while this is not needed for the other two stackings that result constructed consistently.
420 The BB and the NN stacking geometries keep the in-plane order-2 rotations axes along $[10]$.
421 Therefore their layer group is also the $p321$. However, in the BN stacking case, the coincident
422 atoms are now chemically different and the order-2 rotations are lost. The group is the simplest
423 hexagonal $p3$.

424 The last two hBN moiré stackings are the $BBNN(q, p)$ and the $BNNB(q, p)$ which correspond
425 geometrically to the graphene *double* sublattice coincidence moiré. Again, we translate the
426 structures to locate the “hexagon-on-hexagon” vertical axis at the origin. A careful observation
427 of the $BNNB(q, p)$ moiré geometry allows us to notice that the in-plane order-2 rotation axes
428 along $[10]$ and passing through the origin are conserved. The layer group of the BNNB moiré
429 stacking is then again the $p321$. Differently, in the $BBNN(q, p)$ structure, the in-plane order-2
430 rotation axes that are preserved are oriented along the $[11]$ crystallographic directions. The
431 layer group of symmetry of BBNN stacking is then the $p312$.

432 In this work, we have built structures paying attention to preserve the vertical atomic co-
433 incidence, and consequently the order-3 rotation axes. However, we can ask ourselves what
434 happens if we stack a (p, q) or a $(-q, p + q)$ supercell on a (q, p) cell with a totally random
435 translation between the layers. In this scenario, all the point symmetry operations are lost,
436 and only the translations are preserved by construction. This implies that, although the su-
437 percell vectors have the same length and span an angle of 60° , the crystal system is no longer
438 hexagonal. It is *oblique* and the layer group is the simplest $p1$. In the reciprocal plane, only the
439 $+\mathbf{k}/-\mathbf{k}$ symmetry is conserved, and consequently the high-symmetry points K are no longer
440 equivalent.

441 **G Computational details**

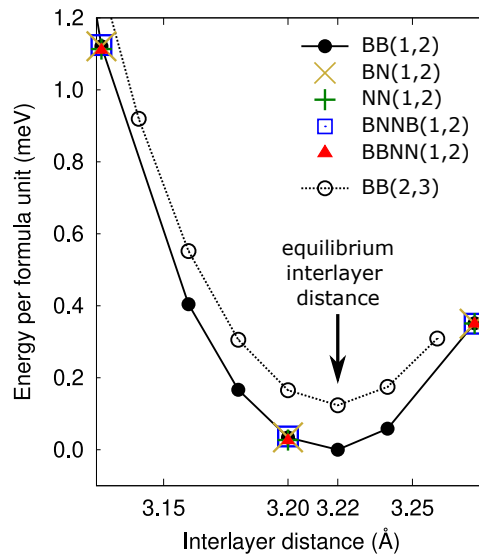


Figure 10: Total energy calculation of the five stackings in the (1,2) supercell as a function of the interlayer distance h . The BB(1,2) is the full black line with black bullets and the BB(2,3) is the dotted line with empty circles. The other (1,2) stackings are superimposed to the BB(1,2) curve almost exactly and are reported with different colors and symbols.

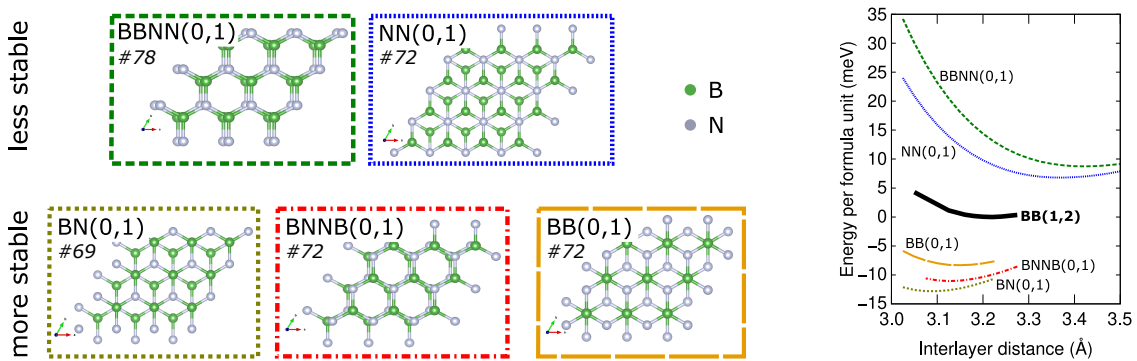


Figure 11: The five hexagonal stackings in untwisted bilayers, their symmetry layer group (#) and their stability curves with respect to the BB(1,2) twisted bilayer.

442 Calculations have been done with the free simulation packages Quantum ESPRESSO [57,
 443 58] (band structure of twisted bilayers) and ABINIT [59,60] (stability of twisted and untwisted
 444 bilayers).

445 In both cases norm-conserving pseudopotentials have been used. We checked that switch-
 446 ing from one software to the other was not introducing major errors in the main characteristics
 447 discussed in the paper. In both groups of calculations, the cutoff energy was 30 Ha and we
 448 sampled the Brillouin zone with a Monkhorst-Pack grid of $5 \times 5 \times 1$ k-points in all supercells
 449 ($9 \times 9 \times 1$ in the untwisted cases). We used the PBE exchange correlation potential [61] and in-
 450 cluded van der Waals corrections via the Grimme-D2 scheme [62]. The equilibrium interlayer
 451 distance has been fixed at 3.22 Å in all bilayers as detailed below. The in-plane cell param-
 452 eter was $a = 2.23$ Å and no in-plane relaxation has been done. A cell height $L = 15$ Å has
 453 been used in all calculations unless specified differently. This value has been fixed by paying

454 attention to the alignment of the σ and π conduction bands. In fact, as already pointed out
455 by several authors [15, 46–51] the bottom conduction in Γ is composed of nearly-free-electron
456 (NFE) states that extend for several Ångströms above the layer and thus converge very slowly
457 with the amount of vacuum (Appendix I).

458 To fix the interlayer distance, we calculated the total energy per unit formula $E(h)$ at dif-
459 ferent input values of the interlayer distance h . Results are reported in Figure 10. We took the
460 BB(1,2) and the BB(2,3) bilayers as reference structures. For these bilayers, we sampled h on
461 a fine grid. Both bilayers have the energy minimum at $h = 3.22$ Å, with a negligible energy
462 difference (~ 0.1 meV per formula unit). Then we computed $E(h)$ for the BN(1,2), NN(1,2),
463 BNNB(1,2) and BBNN(1,2) bilayers on a coarser grid and found that the points fell basically
464 on top of the BB(1,2) curve. Following this analysis, we deduced that we can safely fix the
465 equilibrium distance at $h = 3.22$ Å irrespective of the stacking or the twist angle. We note
466 however that this value may be inaccurate for very small twist angles that are not investigated
467 in this work.

468 H Untwisted bilayers

469 It is possible to extend the nomenclature we introduced in the main text to untwisted bilayers.
470 In this case, only the stacking label is meaningful, the (q, p) pair being trivially 0 and 1. Note
471 however that at fixed stacking, the symmetry group of the untwisted bilayers (reported in
472 Figure 11) differ from that of the twisted ones. In Figure 11 we report an image of the structure
473 of the five untwisted stackings and their stability curve $E(h)$ together with that of the BB(1,2)
474 bilayer. We observe that the three most stable untwisted structures, i.e. the BN(0,1), the
475 BNNB(0,1) and the BB(0,1) have a smaller equilibrium distance, whereas for the two most
476 unstable, the NN(0,1) and the BBNN(0,1), the equilibrium h is larger, so that the twisted
477 bilayers fall somewhat between the two groups. This makes sense if one reckons that inside
478 the same twisted bilayer one can find domains with a local stacking intermediate to the five
479 untwisted ones.

480 In experiments it is observed that, far from certain angles, it is pretty easy to move or twist
481 a BN flake on top of another, and this is consistent with the negligible energy differences we
482 calculated between different stackings at fixed angle and between the two reference calcu-
483 lations with the same stacking sequence. However when the twist angle gets close to some
484 specific values, the flake gets stuck and no further twist is possible. In fact, the large energy
485 differences with the untwisted configurations (order of 10 meV per unit formula) suggest that
486 when approaching small twist angles the bilayer falls into one of the energetically more favor-
487 able configurations, possibly undergoing large in-plane deformation to maximize the size of
488 the untwisted domains. [30, 53, 54, 63].

489 The equilibrium distances, the total energy per BN pair with respect to the BB(1,2) bilayer
490 and the values of the DFT direct (at K) and indirect band gaps (between valleys close to K and
491 the point M) are reported in Table 5.

492 **I Nearly-free-electron states**

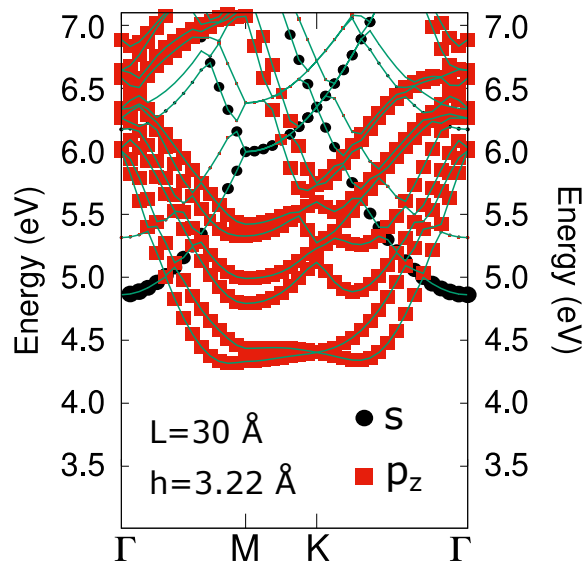


Figure 12: Orbital momentum component of the conduction bands of the BN(1,2) bilayer (fat bands).

493 As already pointed out by Blase and coworkers in the case of bulk hBN [15], the conduc-
 494 tion states at Γ converge very slowly with the amount of vacuum because they correspond to
 495 some unoccupied N-centered nearly-free-electron (NFE) state extending for several Ångströms
 496 above the BN layer [15,46–51]. These NFE states have a neat 3s orbital component, as shown
 497 in the fat-band plot reported in Figure 12.

498 Their alignment with respect to the π bands is a delicate issue on the purpose of this article
 499 because the energy difference between the bottom of the unoccupied σ band and the bottom
 500 of the unoccupied π band are very close in energy and they may compete in determining the
 501 indirect nature of the gap. Therefore, it is worth paying much attention to their convergence.
 502 To this aim, we made a series of two test calculations in a BN(1,2) bilayer. First we tested the
 503 evolution of these states as a function of the height of the simulation cell at fixed interlayer
 504 distance (the three panels of Figure 13.a). This test shows that by reducing the cell height,
 505 the NFE states are pushed toward higher energies because of fictitious cell-to-cell interactions.
 506 Replicas of the system must be separated of around $L \sim 20$ Å for the band dispersion and
 507 alignment to be converged. Note that we decided on purpose to carry out our simulations with

Table 5: Equilibrium interlayer distance h (Å), total energy per formula unit E_{BN} with respect to the BB(1,2) bilayer (in meV), smallest indirect gap E_{ind} (eV) and energy of the smallest direct transition E_{dir} (eV) (direct gap).

System	h	E_{BN}	E_{ind}	E_{dir}
BBNN(0,1)	3.425	8.7	3.957	4.037
NN(0,1)	3.375	6.8	4.345	4.037
BB(2,3)	3.220	0.1	4.217	4.251
BB(1,2)	3.220	0	4.318	4.394
BB(0,1)	3.150	-8.3	3.950	4.436
BNNB(0,1)	3.125	-11.1	4.649	4.398
BN(0,1)	3.100	-12.8	4.463	4.438

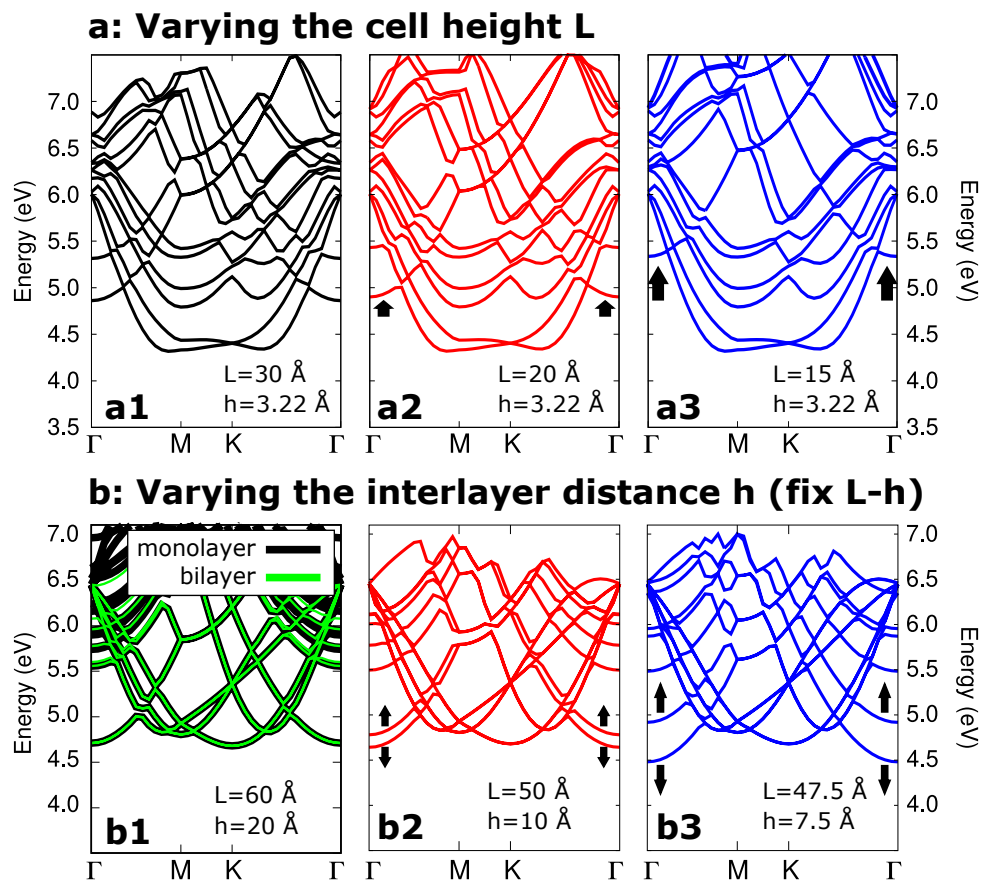


Figure 13: The evolution of the NFE states as a function of the simulation parameters in the BN(1,2) bilayer. **a**: evolution as a function of the cell height L at fixed interlayer distance ($h = 3.22 \text{ \AA}$). $L = 30, 20$ and 15 \AA in panels **a1**, **a2** and **a3** respectively. **b**: evolution as a function of the interlayer distance h at fixed vacuum ($L - h = 40 \text{ \AA}$). $h = 20, 10$ and 7.5 \AA in panels **b1**, **b2** and **b3** respectively. In panel **b1**, the band structure of the BN(1,2) bilayer (flashy green) is compared with that of the isolated monolayer (black).

508 a slightly lower value (15 \AA) because the fact of pushing the NFE states to higher energies is
 509 not detrimental to our investigation and allows us to reduce the computational workload.

510 Then we tested the evolution of the NFE states as a function of the interlayer distance
 511 leaving a constant amount of vacuum ($L - h$) of 40 \AA , which is largely enough to prevent cell-
 512 to-cell interactions. In the panels of Figure 13.b, we report three calculations of the BN(1,2)
 513 bilayer with a varying interlayer distance ($20, 10$ and 7.5 \AA respectively in panels **b1**, **b2** and
 514 **b3**). In the **b1** panel, we also plot in black the conduction band of the isolated monolayer in
 515 the (1,2) supercell and we verify that it coincides with the $h = 20 \text{ \AA}$ bilayer calculation. This
 516 test demonstrates that moving two layers closer to each other induces a bonding/antibonding
 517 splitting of the NFE states which increases as the layers get closer.

518 Since there is no difference between the interlayer distance separating two layers inside
 519 the cell and the space separating replicas of the simulated system, one should pay attention
 520 that these two effects (pushing to higher energies and band splitting) happen at the same time.

521 **J Band gap of the $\delta = 2$ family**

522 In the main text we give the values of the gapwidth of the five stackings of the (1,3) and
 523 (3,5) supercells. The values have been extracted from the corresponding band plots, so they
 524 refer to gapwidths calculated along specific high symmetry paths in the Brillouin zone. In
 525 this section we report a more complete mapping of the band structure of the top valence and
 526 bottom conduction of the BN stacking, chosen as representative of the bilayers. In Figure 14
 527 we report the energy surface of the highest occupied states and the lowest unoccupied states in
 528 the BN(1,3) and BN(3,5) bilayers. With this analysis we demonstrate that the values reported
 529 in the main text are meaningful because the bottom of the conduction and the top of the
 530 valence fall indeed on the high symmetry lines.

531 For this analysis we acknowledge F. Paleari who kindly provided us with a dedicated anal-
 532 ysis post-processing tool.

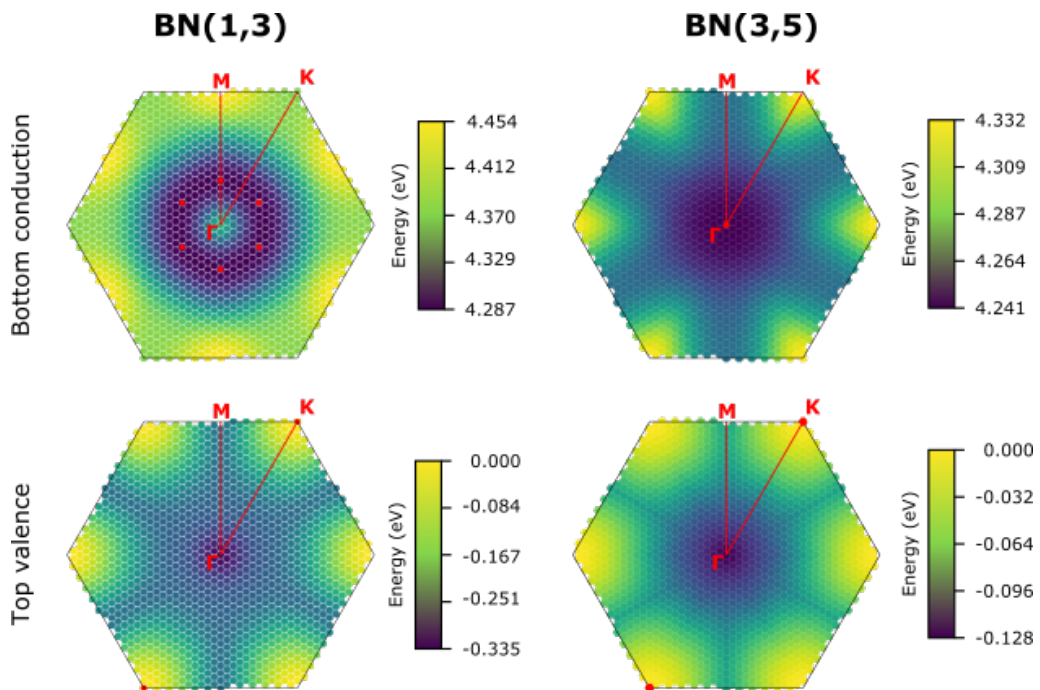


Figure 14: Energy surface of the lowest empty band (top panels) and the highest occupied band (bottom panels) of the BN(1,3) and the BN(3,5) bilayers from left to right. The top valence and the bottom conduction states are highlighted with red hexagons.

533 **K Band structure of the other stackings**

534 Here below we report the band plots missing in the main text corresponding to stackings BBNN,
 535 BB and BNNB from top to bottom.

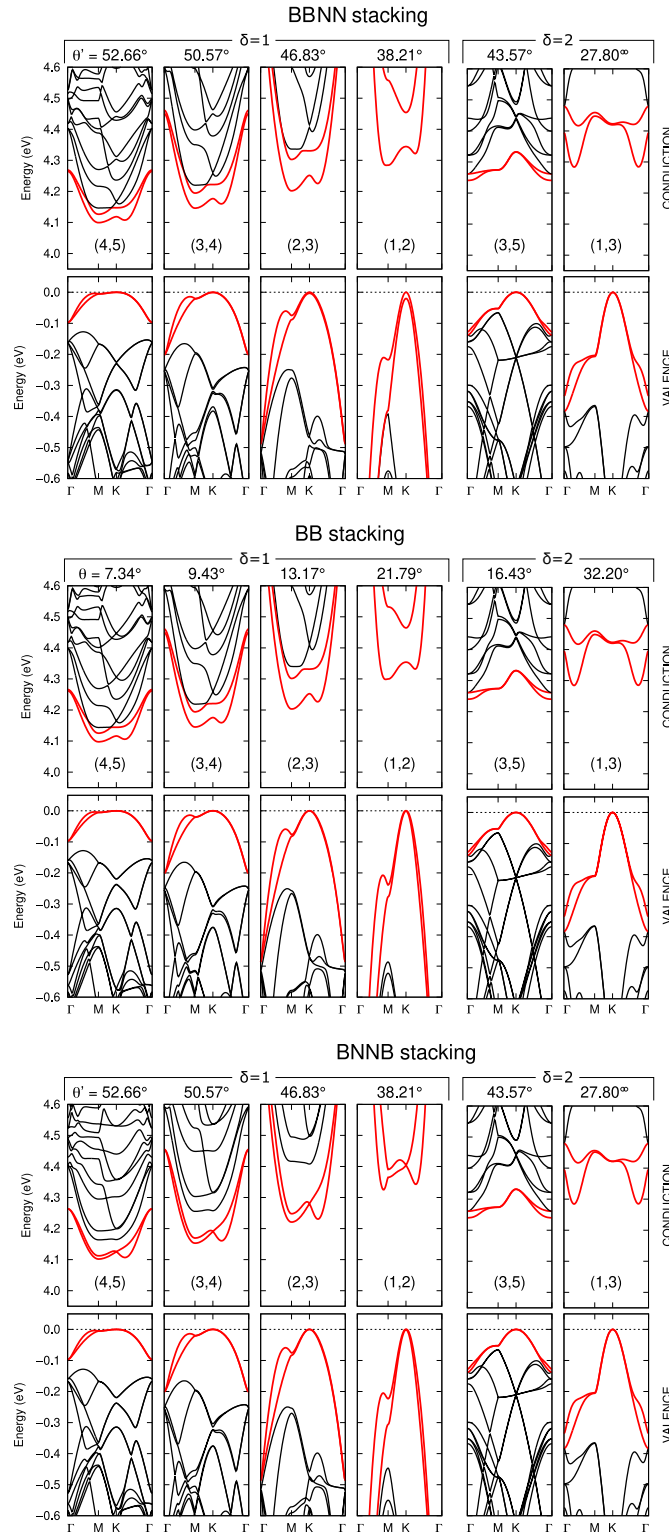


Figure 15: Band structure as a function of the twist angle of the BBNN, BB and BNNB stackings from top to bottom.

536 **References**

- 537 [1] S. Carr, S. Fang and E. Kaxiras, *Electronic-structure methods for twisted moiré layers*, Nat.
538 Rev. Mater. **5**, 748 (2020), doi:[10.1038/s41578-020-0214-0](https://doi.org/10.1038/s41578-020-0214-0).
- 539 [2] E. Suárez Morell, J. D. Correa, P. Vargas, M. Pacheco and Z. Barticevic, *Flat bands in*
540 *slightly twisted bilayer graphene: Tight-binding calculations*, Phys. Rev. B **82**, 121407
541 (2010), doi:[10.1103/PhysRevB.82.121407](https://doi.org/10.1103/PhysRevB.82.121407).
- 542 [3] R. Bistritzer and A. H. MacDonald, *Moiré bands in twisted double-layer graphene*, Proc.
543 Natl. Acad. Sci. U.S.A. **108**, 12233 (2011), doi:[10.1073/pnas.1108174108](https://doi.org/10.1073/pnas.1108174108).
- 544 [4] L. Balents, C. R. Dean, D. K. Efetov and A. F. Young, *Superconductivity and strong corre-*
545 *lations in moiré flat bands*, Nat. Phys. **16**, 725 (2020), doi:[10.1038/s41567-020-0906-9](https://doi.org/10.1038/s41567-020-0906-9).
- 546 [5] D. M. Kennes et al., *Moiré heterostructures as a condensed-matter quantum simulator*, Nat.
547 Phys. **17**, 155 (2021), doi:[10.1038/s41567-020-01154-3](https://doi.org/10.1038/s41567-020-01154-3).
- 548 [6] B. Liu, L. Xian, H. Mu, G. Zhao, Z. Liu, A. Rubio and Z. F. Wang, *Higher-order*
549 *band topology in twisted moiré superlattice*, Phys. Rev. Lett. **126**, 066401 (2021),
550 doi:[10.1103/PhysRevLett.126.066401](https://doi.org/10.1103/PhysRevLett.126.066401).
- 551 [7] J. Choi et al., *Twist angle-dependent interlayer exciton lifetimes in*
552 *van der Waals heterostructures*, Phys. Rev. Lett. **126**, 047401 (2021),
553 doi:[10.1103/PhysRevLett.126.047401](https://doi.org/10.1103/PhysRevLett.126.047401).
- 554 [8] E. M. Alexeev et al., *Resonantly hybridized excitons in moiré superlattices in van der Waals*
555 *heterostructures*, Nature **567**, 81 (2019), doi:[10.1038/s41586-019-0986-9](https://doi.org/10.1038/s41586-019-0986-9).
- 556 [9] C. Jin et al., *Observation of moiré excitons in WSe₂/WS₂ heterostructure superlattices*,
557 Nature **567**, 76 (2019), doi:[10.1038/s41586-019-0976-y](https://doi.org/10.1038/s41586-019-0976-y).
- 558 [10] K. L. Seyler, P. Rivera, H. Yu, N. P. Wilson, E. L. Ray, D. G. Mandrus, J. Yan, W. Yao and
559 X. Xu, *Signatures of moiré-trapped valley excitons in MoSe₂/WSe₂ heterobilayers*, Nature
560 **567**, 66 (2019), doi:[10.1038/s41586-019-0957-1](https://doi.org/10.1038/s41586-019-0957-1).
- 561 [11] K. Tran et al., *Evidence for moiré excitons in van der Waals heterostructures*, Nature **567**,
562 71 (2019), doi:[10.1038/s41586-019-0975-z](https://doi.org/10.1038/s41586-019-0975-z).
- 563 [12] F. Wu, T. Lovorn, E. Tutuc, I. Martin and A. H. MacDonald, *Topological insulators*
564 *in twisted transition metal dichalcogenide homobilayers*, Phys. Rev. Lett. **122**, 086402
565 (2019), doi:[10.1103/PhysRevLett.122.086402](https://doi.org/10.1103/PhysRevLett.122.086402).
- 566 [13] D. A. Ruiz-Tijerina and V. I. Fal'ko, *Interlayer hybridization and moiré superlattice mini-*
567 *bands for electrons and excitons in heterobilayers of transition-metal dichalcogenides*, Phys.
568 Rev. B **99**, 125424 (2019), doi:[10.1103/PhysRevB.99.125424](https://doi.org/10.1103/PhysRevB.99.125424).
- 569 [14] H. Ochoa and A. Asenjo-Garcia, *Flat bands and chiral optical response of moiré insulators*,
570 Phys. Rev. Lett. **125**, 037402 (2020), doi:[10.1103/PhysRevLett.125.037402](https://doi.org/10.1103/PhysRevLett.125.037402).
- 571 [15] X. Blase, A. Rubio, S. G. Louie and M. L. Cohen, *Quasiparticle band structure of*
572 *bulk hexagonal boron nitride and related systems*, Phys. Rev. B **51**, 6868 (1995),
573 doi:[10.1103/PhysRevB.51.6868](https://doi.org/10.1103/PhysRevB.51.6868).

- 574 [16] T. Galvani, F. Paleari, H. P. C. Miranda, A. Molina-Sánchez, L. Wirtz, S. Latil, H. Amara
575 and F. Ducastelle, *Excitons in boron nitride single layer*, Phys. Rev. B **94**, 125303 (2016),
576 doi:[10.1103/PhysRevB.94.125303](https://doi.org/10.1103/PhysRevB.94.125303).
- 577 [17] L. Schué, L. Sponza, A. Plaud, H. Bensalah, K. Watanabe, T. Taniguchi, F. Ducastelle, A.
578 Loiseau and J. Barjon, *Bright luminescence from indirect and strongly bound excitons in*
579 *h-BN*, Phys. Rev. Lett. **122**, 067401 (2019), doi:[10.1103/PhysRevLett.122.067401](https://doi.org/10.1103/PhysRevLett.122.067401).
- 580 [18] A. Rousseau et al., *Monolayer boron nitride: Hyperspectral imaging in the deep ultraviolet*,
581 Nano Lett. **21**, 10133 (2021), doi:[10.1021/acs.nanolett.1c02531](https://doi.org/10.1021/acs.nanolett.1c02531).
- 582 [19] T. T. Tran, K. Bray, M. J. Ford, M. Toth and I. Aharonovich, *Quantum emis-*
583 *sion from hexagonal boron nitride monolayers*, Nature Nanotech. **11**, 37 (2015),
584 doi:[10.1038/nnano.2015.242](https://doi.org/10.1038/nnano.2015.242).
- 585 [20] R. Bourrellier, S. Meuret, A. Tararan, O. Stéphan, M. Kociak, L. H. G. Tizei and A. Zobelli,
586 *Bright UV single photon emission at point defects in h-BN*, Nano Lett. **16**, 4317 (2016),
587 doi:[10.1021/acs.nanolett.6b01368](https://doi.org/10.1021/acs.nanolett.6b01368).
- 588 [21] G. Grosso et al., *Tunable and high-purity room temperature single-photon emission*
589 *from atomic defects in hexagonal boron nitride*, Nat. Commun. **8**, 705 (2017),
590 doi:[10.1038/s41467-017-00810-2](https://doi.org/10.1038/s41467-017-00810-2).
- 591 [22] C. Li, Z.-Q. Xu, N. Mendelson, M. Kianinia, M. Toth and I. Aharonovich, *Purification of*
592 *single-photon emission from hBN using post-processing treatments*, Nanophotonics **8**, 2049
593 (2019), doi:[10.1515/nanoph-2019-0099](https://doi.org/10.1515/nanoph-2019-0099).
- 594 [23] M. Fischer et al., *Controlled generation of luminescent centers in hexagonal boron nitride*
595 *by irradiation engineering*, Sci. Adv. **7**, eabe7138 (2021), doi:[10.1126/sciadv.abe7138](https://doi.org/10.1126/sciadv.abe7138).
- 596 [24] F. Libbi, P. Miguel M. C. de Melo, Z. Zanolli, M. Jean Verstraete and N. Marzari, *Phonon-*
597 *assisted luminescence in defect centers from many-body perturbation theory*, Phys. Rev. Lett.
598 **128**, 167401 (2022), doi:[10.1103/physrevlett.128.167401](https://doi.org/10.1103/physrevlett.128.167401).
- 599 [25] L. Britnell et al., *Electron tunneling through ultrathin boron nitride crystalline barriers*,
600 Nano Lett. **12**, 1707 (2012), doi:[10.1021/nl3002205](https://doi.org/10.1021/nl3002205).
- 601 [26] M. P. Levendorf, C.-J. Kim, L. Brown, P. Y. Huang, R. W. Havener, D. A. Muller and J. Park,
602 *Graphene and boron nitride lateral heterostructures for atomically thin circuitry*, Nature
603 **488**, 627 (2012), doi:[10.1038/nature11408](https://doi.org/10.1038/nature11408).
- 604 [27] S. K. Jang, J. Youn, Y. Jae Song and S. Lee, *Synthesis and characterization of hexagonal*
605 *boron nitride as a gate dielectric*, Sci. Rep. **6**, 30449 (2016), doi:[10.1038/srep30449](https://doi.org/10.1038/srep30449).
- 606 [28] T. Knobloch et al., *The performance limits of hexagonal boron nitride as an insulator for*
607 *scaled CMOS devices based on two-dimensional materials*, Nat. Electron. **4**, 98 (2021),
608 doi:[10.1038/s41928-020-00529-x](https://doi.org/10.1038/s41928-020-00529-x).
- 609 [29] K. Yasuda, X. Wang, K. Watanabe, T. Taniguchi and P. Jarillo-Herrero, *Stacking-*
610 *engineered ferroelectricity in bilayer boron nitride*, Science **372**, 1458 (2021),
611 doi:[10.1126/science.abd3230](https://doi.org/10.1126/science.abd3230).
- 612 [30] C. R. Woods et al., *Charge-polarized interfacial superlattices in marginally twisted hexago-*
613 *nal boron nitride*, Nat. Commun. **12**, 347 (2021), doi:[10.1038/s41467-020-20667-2](https://doi.org/10.1038/s41467-020-20667-2).

- 614 [31] F. Paleari, T. Galvani, H. Amara, F. Ducastelle, A. Molina-Sánchez and L. Wirtz, *Excitons*
615 *in few-layer hexagonal boron nitride: Davydov splitting and surface localization*, 2D Mater.
616 **5**, 045017 (2018), doi:[10.1088/2053-1583/aad586](https://doi.org/10.1088/2053-1583/aad586).
- 617 [32] H. Y. Lee, M. M. Al Ezzi, N. Raghuvanshi, J. Yang Chung, K. Watanabe, T. Taniguchi, S.
618 Garaj, S. Adam and S. Gradečak, *Tunable optical properties of thin films controlled by the*
619 *interface twist angle*, Nano Lett. **21**, 2832 (2021), doi:[10.1021/acs.nanolett.0c04924](https://doi.org/10.1021/acs.nanolett.0c04924).
- 620 [33] X.-J. Zhao, Y. Yang, D.-B. Zhang and S.-H. Wei, *Formation of Bloch flat bands in*
621 *polar twisted bilayers without magic angles*, Phys. Rev. Lett. **124**, 086401 (2020),
622 doi:[10.1103/PhysRevLett.124.086401](https://doi.org/10.1103/PhysRevLett.124.086401).
- 623 [34] G. Trambly de Laissardière, D. Mayou and L. Magaud, *Localization of Dirac electrons in*
624 *rotated graphene bilayers*, Nano Lett. **10**, 804 (2010), doi:[10.1021/nl902948m](https://doi.org/10.1021/nl902948m).
- 625 [35] L. Xian, D. M. Kennes, N. Tancogne-Dejean, M. Altarelli and A. Rubio, *Multiflat bands and*
626 *strong correlations in twisted bilayer boron nitride: Doping-induced correlated insulator and*
627 *superconductor*, Nano Lett. **19**, 4934 (2019), doi:[10.1021/acs.nanolett.9b00986](https://doi.org/10.1021/acs.nanolett.9b00986).
- 628 [36] X.-J. Zhao, Y. Yang, D.-B. Zhang and S.-H. Wei, *Flat bands in twisted bilayers*
629 *of polar two-dimensional semiconductors*, Phys. Rev. Mater. **5**, 014007 (2021),
630 doi:[10.1103/PhysRevMaterials.5.014007](https://doi.org/10.1103/PhysRevMaterials.5.014007).
- 631 [37] L. Wirtz, A. Marini and A. Rubio, *Excitons in boron nitride nanotubes: Dimensionality*
632 *effects*, Phys. Rev. Lett. **96**, 126104 (2006), doi:[10.1103/PhysRevLett.96.126104](https://doi.org/10.1103/PhysRevLett.96.126104).
- 633 [38] L. Sponza, H. Amara, C. Attaccalite, S. Latil, T. Galvani, F. Paleari, L. Wirtz and
634 F. Ducastelle, *Direct and indirect excitons in boron nitride polymorphs: A story of*
635 *atomic configuration and electronic correlation*, Phys. Rev. B **98**, 125206 (2018),
636 doi:[10.1103/PhysRevB.98.125206](https://doi.org/10.1103/PhysRevB.98.125206).
- 637 [39] J. C. G. Henriques, B. Amorim, R. M. Ribeiro and N. M. R. Peres, *Excitonic re-*
638 *sponse of AA' and AB stacked hBN bilayers*, Phys. Rev. B **105**, 115421 (2022),
639 doi:[10.1103/PhysRevB.105.115421](https://doi.org/10.1103/PhysRevB.105.115421).
- 640 [40] A. N. Kolmogorov and V. H. Crespi, *Registry-dependent interlayer potential for graphitic*
641 *systems*, Phys. Rev. B **71**, 235415 (2005), doi:[10.1103/PhysRevB.71.235415](https://doi.org/10.1103/PhysRevB.71.235415).
- 642 [41] E. J. Mele, *Commensuration and interlayer coherence in twisted bilayer graphene*, Phys.
643 Rev. B **81**, 161405 (2010), doi:[10.1103/PhysRevB.81.161405](https://doi.org/10.1103/PhysRevB.81.161405).
- 644 [42] K. A. Mengle and E. Kioupakis, *Impact of the stacking sequence on the bandgap and lumi-*
645 *nescence properties of bulk, bilayer, and monolayer hexagonal boron nitride*, APL Materials
646 **7**, 021106 (2019), doi:[10.1063/1.5087836](https://doi.org/10.1063/1.5087836).
- 647 [43] S. M. Gilbert et al., *Alternative stacking sequences in hexagonal boron nitride*, 2D Mater.
648 **6**, 021006 (2019), doi:[10.1088/2053-1583/ab0e24](https://doi.org/10.1088/2053-1583/ab0e24).
- 649 [44] G. Trambly de Laissardière, D. Mayou and L. Magaud, *Numerical studies of con-*
650 *fined states in rotated bilayers of graphene*, Phys. Rev. B **86**, 125413 (2012),
651 doi:[10.1103/PhysRevB.86.125413](https://doi.org/10.1103/PhysRevB.86.125413).
- 652 [45] S. Shallcross, S. Sharma, E. Kandelaki and O. A. Pankratov, *Electronic structure of tur-*
653 *bostratic graphene*, Phys. Rev. B **81**, 165105 (2010), doi:[10.1103/PhysRevB.81.165105](https://doi.org/10.1103/PhysRevB.81.165105).

- 654 [46] M. Posternak, A. Baldereschi, A. J. Freeman, E. Wimmer and M. Weinert, *Prediction of*
655 *electronic interlayer states in graphite and reinterpretation of alkali bands in graphite inter-*
656 *calation compounds*, Phys. Rev. Lett. **50**, 761 (1983), doi:[10.1103/PhysRevLett.50.761](https://doi.org/10.1103/PhysRevLett.50.761).
- 657 [47] M. Posternak, A. Baldereschi, A. J. Freeman and E. Wimmer, *Prediction of elec-*
658 *tronic surface states in layered materials: Graphite*, Phys. Rev. Lett. **52**, 863 (1984),
659 doi:[10.1103/PhysRevLett.52.863](https://doi.org/10.1103/PhysRevLett.52.863).
- 660 [48] X. Blase, L. X. Benedict, E. L. Shirley and S. G. Louie, *Hybridization effects and*
661 *metallicity in small radius carbon nanotubes*, Phys. Rev. Lett. **72**, 1878 (1994),
662 doi:[10.1103/PhysRevLett.72.1878](https://doi.org/10.1103/PhysRevLett.72.1878).
- 663 [49] X. Blase, A. Rubio, S. G. Louie and M. L. Cohen, *Stability and band gap constancy of boron*
664 *nitride nanotubes*, Europhys. Lett. **28**, 335 (1994), doi:[10.1209/0295-5075/28/5/007](https://doi.org/10.1209/0295-5075/28/5/007).
- 665 [50] S. Hu, J. Zhao, Y. Jin, J. Yang, H. Petek and J. G. Hou, *Nearly free electron su-*
666 *peratom states of carbon and boron nitride nanotubes*, Nano Lett. **10**, 4830 (2010),
667 doi:[10.1021/nl1023854](https://doi.org/10.1021/nl1023854).
- 668 [51] F. Paleari, *First-principles approaches to the description of indirect absorption and lumi-*
669 *nescence spectroscopy: Exciton-phonon coupling in hexagonal boron nitride*, Ph.D. thesis,
670 University of Luxembourg, Luxembourg, (2019).
- 671 [52] N. Berseneva, A. Gulans, A. V. Krasheninnikov and R. M. Nieminen, *Electronic structure of*
672 *boron nitride sheets doped with carbon from first-principles calculations*, Phys. Rev. B **87**,
673 035404 (2013), doi:[10.1103/PhysRevB.87.035404](https://doi.org/10.1103/PhysRevB.87.035404).
- 674 [53] F. Guinea and N. R. Walet, *Continuum models for twisted bilayer graphene: Effect*
675 *of lattice deformation and hopping parameters*, Phys. Rev. B **99**, 205134 (2019),
676 doi:[10.1103/PhysRevB.99.205134](https://doi.org/10.1103/PhysRevB.99.205134).
- 677 [54] N. R. Walet and F. Guinea, *Flat bands, strains, and charge distribution in twisted bilayer*
678 *h-BN*, Phys. Rev. B **103**, 125427 (2021), doi:[10.1103/PhysRevB.103.125427](https://doi.org/10.1103/PhysRevB.103.125427).
- 679 [55] S. L. Moore et al., *Nanoscale lattice dynamics in hexagonal boron nitride moiré superlat-*
680 *tices*, Nat. Commun. **12**, 5741 (2021), doi:[10.1038/s41467-021-26072-7](https://doi.org/10.1038/s41467-021-26072-7).
- 681 [56] V. Kopsky and D. Litvin, *International tables for crystallography, Volume E: Subperiodic*
682 *groups*, Springer, Heidelberg, Germany, ISBN 9781402007156 (2002).
- 683 [57] P. Giannozzi et al., *QUANTUM ESPRESSO: A modular and open-source software project*
684 *for quantum simulations of materials*, J. Phys.: Condens. Matter **21**, 395502 (2009),
685 doi:[10.1088/0953-8984/21/39/395502](https://doi.org/10.1088/0953-8984/21/39/395502).
- 686 [58] P. Giannozzi et al., *Advanced capabilities for materials modelling with QUANTUM*
687 *ESPRESSO*, J. Phys.: Condens. Matter **29**, 465901 (2017), doi:[10.1088/1361-](https://doi.org/10.1088/1361-648x/aa8f79)
688 [648x/aa8f79](https://doi.org/10.1088/1361-648x/aa8f79).
- 689 [59] X. Gonze et al., *The ABINIT project: Impact, environment and recent developments*, Com-
690 put. Phys. Commun. **248**, 107042 (2020), doi:[10.1016/j.cpc.2019.107042](https://doi.org/10.1016/j.cpc.2019.107042).
- 691 [60] A. H. Romero et al., *ABINIT: Overview and focus on selected capabilities*, J. Chem. Phys.
692 **152**, 124102 (2020), doi:[10.1063/1.5144261](https://doi.org/10.1063/1.5144261).
- 693 [61] J. P. Perdew, K. Burke and M. Ernzerhof, *Generalized gradient approximation made simple*,
694 Phys. Rev. Lett. **77**, 3865 (1996), doi:[10.1103/PhysRevLett.77.3865](https://doi.org/10.1103/PhysRevLett.77.3865).

- 695 [62] S. Grimme, *Semiempirical GGA-type density functional constructed with a long-range dis-*
696 *persion correction*, J. Comput. Chem. **27**, 1787 (2006), doi:[10.1002/jcc.20495](https://doi.org/10.1002/jcc.20495).
- 697 [63] K. Yao et al., *Enhanced tunable second harmonic generation from twistable interfaces*
698 *and vertical superlattices in boron nitride homostructures*, Sci. Adv. **7**, eabe8691 (2021),
699 doi:[10.1126/sciadv.abe8691](https://doi.org/10.1126/sciadv.abe8691).